UNIVERSITY OF COPENHAGEN

Clara Celeste Qvotrup

Deflecting waveguides for three-dimensional quantum photonic integrated circuits

Master thesis

19.06.2021

Main supervisor: Assoc. Prof. Leonardo Midolo

Co-supervisors: Prof. Peter Lodahl, Zhe Liu

Abstract

Integrated photonic circuits provide a promising platform for quantum information processing. However, effective integrated photonics require an efficient method of chip-to-fiber coupling, and a method which is both scalable, effective and broadband have yet to be developed.

In this thesis, a novel three-dimensional cantilever waveguide working as a hybrid coupler is introduced. By exploiting the intrinsic stress mismatch between the GaAs wafer and Nickel strips placed on the chip by metal evaporation, bilayer cantilever waveguides with a circular curvatures are realized, containing a radius of curvature dependent on the stress mismatch. By tailoring the length of the cantilever, the orientation of the epoxy-clad cantilever tip can be calibrated to reach a 90 degree angle with the substrate. In this configuration the epoxy-clad waveguide tip acts as a coupler, allowing for vertical in and out-coupling of light from the top window of a cryostat.

The fabrication process of the device is described, as well as an introduction to the complex behavior of strained semi-conductors. Using the finite element method software COMSOL, simulations of the piezo-electric response of the bent bilayer cantilever to an applied electric potential are carried out, and used to describe the potential for strain tuning of GaAs quantum dots embedded in the waveguide. Furthermore, simulations of a flat bilayer cantilever with intrinsic stress on Nickel layer are run, and the resulting strain in the curved waveguide extracted. Using this strain, theoretical models for the changes in optical properties due to respectively band gap change described by the Pikus-Bir Hamiltonian and sub-bandgap absorption due to the Franz-Keldysh effect from the electric fields induced by the piezo- and flexoelectric effect are described.

The fabricated chip is placed in a flow cryostat, and the transmission was characterized for the transverse electric (TE) and transverse magnetic (TM) modes at 10 K and 293 K. The bent cantilevers were found to be heat While the efficiency for the bent cantilever waveguide coupler is 1low, it was found to be extremely broadband, with full-width half-maximum bandwidths over 150 nm being observed for both the TM and TE modes.

During characterization, an abrupt cutoff allowing no transmission for wavelengths below it was found. This cutoff greatly differed between the TE and TM modes (935 nm for TE vs 905 nm for TM at room temperature), and was similarly found to be greatly temperature dependent. By taking measurements for the TE transmission for a wide range of temperatures in the range of 293 - 10 K, the temperature dependence of the cutoff, $E_{cut}(T)$ was found. Comparing this cutoff to the temperature-dependent GaAs bandgap, $E_g(T)$, it was found that they followed exactly the same slope, but differed with an offset of $E_{change} = E_{cut}(T) - E_g(T) \approx -0.10\,\text{eV}$. The possible configurations of strain causing this bandgap was investigated.

Acknowledgements

I would like to extend my sincere gratitude to my main advisor, Prof. Leonardo Midolo, who took me on as a master's student with short notice, and who despite a very busy schedule always found time for me. Thank you for letting me explore the fascinating field of semiconductor materials physics, for giving me the great freedom I had in shaping this thesis, and for reminding me when it was time to get back on track.

Thank you to Zhe Liu, for patiently teaching me the ins and outs of nanofabrication, and for fabricating my final sample when another of my own failed and the time was getting critical.

Thanks to Camille Papon, whose role have almost been that of an unofficial advisor. Your help and support, in and out of the laboratory was invaluable. Thank you Beatrice de Lio for your assistance in the lab. I'd also like to thank the entire Quantum Photonics group and the HyQ center for creating a friendly, open and informal environment, even in these interesting times. Last but not least, I would like to thank those closest to me. I would like to thank my parents, Mie and Troels for their endless support throrough this thesis period, but also my entire life. To my boyfriend Emil, thank you for being you. You are a constant source of joy and stability for me and thanks to you I can keep going even in my darkest times.

Contents

Chapter 1

Introduction

The invention of early programmable digital computers, such as the ENIAC which was completed in 1945, marked a revolution. The ENIAC allowed ballistic trajectories, which could take a human 20 hours to calculate by hand, to be calculated in half a minute[12]. However the early computers were large and cumbersome, consisting of thousands of vaccuum tubes which added to complexity of troubleshooting. Eventually, early computers reached a complexity level where the downtime spent on repairs and troubleshooting outweighed the advantage of faster computational power. While technological advances made the individual component smaller and more reliable, the connection between components were still unreliable, and the smaller size and denser packing of components brought additional challenges during repair and replacement of parts.

The invention of semiconductor electronic integrated circuits (EICs) during the late fifties solved many of these problems. With many components seamlessly integrated on one chip unreliable connections between discrete components could be avoided. Furthermore, innovations in microfabrication allowed for smaller and denser packaged components, allowing for ever stronger computational power in rapidly shrinking digital devices.

Photonic integrated circuits (PICs) can be thought of as analogous to electronic integrated circuits, but utilizing optical signals rather than electrical. Like EICs, PICs greatly benefits from the reliability and efficiency inherent to integrated circuits. Currently, PICs are used in telecommunications to facilitate high-speed optical communication while keeping power use low [6].

Micro- and nanoscale PICs are additionally the backbone of many technologies in the fields of quantum information processing and quantum simulations[21]. With quantum dots (QDs) serving as reliable and efficient single photon emitters[34], entire photonic systems can be built into one chip. This lays the groundwork for bulding quantum simulators, quantum computers and quantum communication systems.

Effective photonic quantum information processing requires access to a high-purity source of indistinguishable single photons[19]. For this purpose, semiconductor quantum dots have proved to be an efficient type of single photon sources[34]. These nano-size quantum structures can be embedded in the For this purpose, Gallium Arsenide (GaAs) is chosen due to its combination of satisfactory optical properties, as well as its direct bandgap, allowing for embedded quantum dots functioning as single photon sources.

This thesis seeks to explore a novel microphotonic device consisting of cantilever waveguides tethered to a bilayer Gallium Arsenide and Nickel on each side. When the device is released from the underlying substrate, it curls up in an attempt to minimize the intrinsic stress mismatch between the layers[23]. With the length of the cantilever tailored to ensure that it reaches a total curvature of $\pi/2$, the vertical position of the tapered tips allows the waveguide to function as an in- or outcoupler to light.

However, this device is strongly strained, and the disturbances in the crystal lattice leads to

several corrections of material properties, such as change in bandgap and splitting of previously degenerate energy band levels[32], electrical polarization induced by not only local strain but also the strain gradient[11], which in turn can results in smearing of the absorption edge, allowing sub-bandgap absorption[27]. A deep understanding of the complex responses to strain in semiconductor crystals is thus needed.

In chapter 2, the relevant components of the quantum photonic integrated circuit are described, and the novel device is introduced. In chapter 3, an introduction to semiconductor physics and solid mechanics is given, leading to further discussion of the complex material phenomena in strained crystals. In chapter 4, finite method simulations on the intrinsic and piezo-electrically induced strain in the waveguide are carried out, and the resulting material responses are calculated. In chapter 5, techniques and processes for the fabrication of GaAs photonic integrated circuits are described, and in chapter 6, the optical setup is described, and the results of the characterization of transmission through the waveguide are analysed and discussed. Finally, chapter 7 contains discussion and outlook.

Chapter 2

Quantum Photonics

In this chapter, an introduction to the component of the quantum photonic circuit are laid out. The novel device investigated in this thesis is introduced, and the mechanics of the bending are described.

2.1 Components of the Quantum Photonic Integrated Circuit

Integrated quantum photonic circuits has potential to provide a fast and efficient processing of quantum photonic information.

2.1.1 Quantum Dots

A quantum dot is a semiconductor nanostructure confined in all three directions.

Quantum dots are islands of atoms of a semiconductor with a smaller bandgap, artificially grown inside a semiconductor with a larger bandgap. As an example, quantum dots can consist of InAs atoms ($E_{gap} = 0.43$ eV at 0 K) in a GaAs substrate ($E_{gap} = 1.52$ eV at 0 K)[16]. To create those, a wetting layer of InAs a few atoms thick is deposited on top of a GaAs substrate using Molecular Beam Epitaxy (MBE). The 7% lattice mismatch between GaAs and InAs induces a strain in the system. After the wetting layer has reached a critical thickness, which for InAs QDs on GaAs is about 3 layers, the deposited InAs will instead begin to form pyramidally shaped islands at random positions. A final layer of GaAs caps the quantum dots, protecting them from oxidation. Typical dimensions of these self-assembled quantum dots are 15-30 nm in the lateral direction and a height of 3-5 nm. [15]

This technique, which is known as the Stranski-Krastanov mode of thin film growth, results in semiconductor nanostructures which are spatially constricted in all three dimensions. This causes the energy levels in the quantum dot to be discrete, like in a single atom.

2.1.2 Light-Matter Interactions in the Waveguide

A waveguide refers to a structure whose material and physical dimensions allows conduction of waves with certain polarization modes, frequencies and directions, while extinguishing others. Examples of types of waveguides are macroscale hollow metal tubes used to conduct radio waves, optical silica fibers used for high-speed communications and suspended semiconductor structures in photonic circuits. In this thesis, suspended GaAs waveguides are used. The waveguides are

fabricated on a 160 nm thick Gallium Arsenide wafer lying on a sacrificial layer of AlGaAs. During the undercut, the AlGaAs layer is etched away using hydroflouric acid, which suspends the waveguide between sets of tethers keeping it in place. The suspended waveguides can be regarded as a variation of dielectric slab waveguide which consists of three stacked dielectric layers, where the middle layer has a higher index of refraction than the upper and lower layer. For light at high incident angles, this confines the light to the waveguide by total internal reflection.

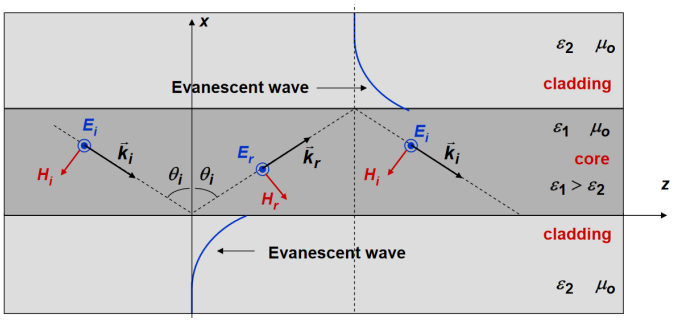

Figure 2.1: Geometric interpretation of a TE mode in a dielectric slab waveguide.[i]

In free space or in a bulk dielectric, both the electric and the magnetic field are perpendicular to the propagation direction and the field can be described as a superposition of plane waves.[27] However, in waveguides the boundary conditions are imposed by the physical structure of the waveguide. In figure 2.1, a geometrical interpretation of a TE mode in a dielectrical slab waveguide can be seen. With the waves being confined by total internal reflection, they propagate by bouncing back and forth at an angle. The electrical field is perpendicular to the propagation direction, while the magnetic field has a component in the direction of propagation.

In this geometrical interpretation, any wave hitting the surface of the waveguide from the inside at an angle higher than the critical angle for total internal reflection will be confined to the waveguide. However, this does not necessarily mean that the wave will be guided. Optical waves undergoing total internal reflection will experience a non-trivial phase shift ϕ. This dephasing of the wave will cause it to interfere destructively with itself unless ϕ causes the wave to be exactly in phase with the waves produced by the earlier reflections.

This resonance condition requires that the total phase acquired during one round trip transverse passage is[18]

$$2k\cos(\theta_i)d + 2\phi(\theta_i) = m2\pi \tag{2.1}$$

where $k = \omega/c$ is the propagation constant, θ_i is the angle of incidence, d is the thickness, ϕ is the phase shift acquired from the total internal reflection and m is the mode number of the guided wave.

At the same time, propagation requires total internal reflection

$$\theta_i > \sin^{-1}\left(\frac{n_2}{n_1}\right) \tag{2.2}$$

By comparing equations 2.1 and 2.2, the allowed modes m for respectively TE and TM can be found. If the waveguide is spatially confined, one can restrict allowed modes to only the two fundamental modes, TE_0 and TM_0

The lowest allowed wavelength in a semiconductor waveguide is decided by the material. Direct bandgab semiconductors will absorb photons with a wavelength less than $\lambda_g = c \cdot h/E_g$, which

[i] https://courses.cit.cornell.edu/ece303/Lectures/lecture26.pdf

facilitates a transition of an electron from the valence band to the conduction band, creating an electron-hole pair. Photons with energies above the bandgap will give off the spare energy as heat, leading to lattice vibrations.

For GaAs waveguides, the TE and TM modes couple differently to the light and heavy hole conduction bands, which are degenerate at the Γ point at the position of the bandgap.[10] The TE mode exclusively excites the HH band, while the TM mode excites the LH band. For the purpose of characterizing the transmittivity of waveguides, the identical bandgap of the LH and HH bands means that the TE and TM modes should have the same lower allowed wavelength. However, as will be described in chapter 3, applied strain can lift this degeneracy and lead to different behavior for the TE and TM modes.

2.1.3 Couplers

Efficient photonic integrated circuits require implementation of a low-loss chip-to-fiber coupling method. Several methods have been developed, which generally falls into either edge (or in-plane) couplers or out-of-plane couplers. The most efficient methods of chip-to-fiber coupling are in-plane coupling, such as inverted tapers, where the optical fiber is placed horizontally besides the chip. This method gives high efficiency and is relatively polarization independent, but places restrictions on the positioning of devices since in-plane couplers must be placed at chip edges, placing constraints on circuit design as well as limiting the number of devices which can be positioned on one chip. This is disadvantageous especially for research purposes, where it is often necessary to fabricate a large number of novel devices with low yield in order to obtain a few working samples.[20]

Out-of-plane coupling, where the light is shone vertically down on etched gratings, are advantageous in cryostates with only top windows. Furthermore, they are advantageous when working with large numbers of devices, devices placed on the middle of the chips, or devices with multiple ports since out-of-plane couplers can be placed anywhere on the chip. It also removes the need for meticulously aligning the mask with the edges of the chip during fabrication. Out-of-plane couplers are also known as grating couplers (GCs), where gratings with the desired depth, angle and distance are etched into the waveguide material.

Due to birefringence in waveguide materials, $n_{TE} \neq n_{TM}$, two GCs optimized for respectively TE and TM modes at the same incident angle and wavelength would require two different distances between the gratings[20]. Furthermore, some types of GCs couple exclusively to the TE or TM mode, making measurements on the other mode impossible.[38] Etched grating couplers are also relatively narrow-band, and the angle of the excitation and collection needs to be optimized for each wavelength, making this type of couplers suboptimal for measurements wherein a broad range of wavelengths are compared.

Depending on the device in question and the experiments needed to be carried out, the fact that simple GCs must be optimized to a single mode can be regarded as either a limitation or a feature. For some purposes it is necessary to know exactly what mode is conducted through the a waveguide with multimode couplers, which can be done by aligning the optical path to the TE or TM mode of waveguide with single mode GCs placed parallel or perpendicular to the waveguide containing multimode couplers.

In this thesis, a device acting as a hybrid coupler is introduced. The device consists of a three-dimensional cantilever bending due to an intrinsic strain mismatch between the GaAs waveguide and metal strips placed on top. This coupler can be placed anywhere, like a grating coupler, but retains the large bandwidth and polarization independence of an edge coupler.

2.1.4 The novel device.

In this thesis, the focus is on describing the properties of a novel device, the three-dimensional bent bilayer cantilever waveguide. By utilizing the intrinsic stress mismatch between the layers in a bilayer cantilever consiting of a Nickel strip on a GaAs wafer lying on a sacrificial layer of AlGaAs.

The Nickel strips are under intrinsic tensile stress due to lattice mismatch between Ni and GaAs. Once the device is finished it will be undercut, meaning that the AlGaAs layer under the cantilevers will be etched away, which frees the waveguide. For a bilayer cantilever where the two layers have different intrinsic strain, meaning that their unstrained lengths are different, the release of the intrinsic stress of the two layers will be constrained at the interface between them. If the lower layer has a longer unstressed length than the upper layer, the release of the stress will cause the bilayer to curl upwards until it reaches a radius of curvature that minimizes the potential energy over the lower device.

If the strain mismatch is known, the radius of curvature can be found as

$$\frac{1}{\rho} = \frac{6\epsilon(1+m)^2}{d[3(1+m)^2 + (1+mn)(m^2+(mn)^{-1})]} \tag{2.3}$$

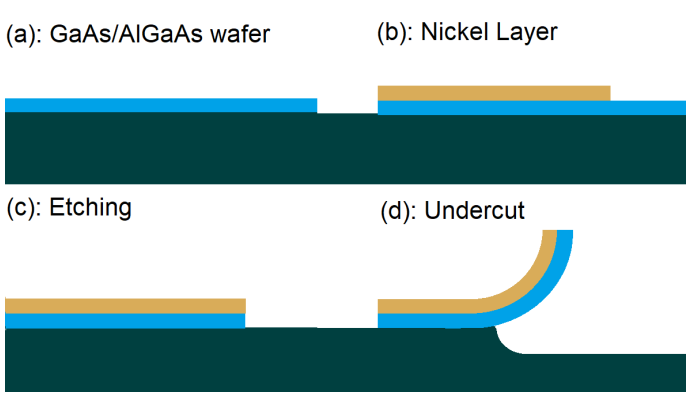

(a) Process of creating a bilayer cantilever.

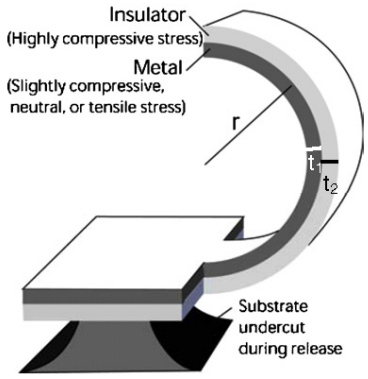

(b) Illustration of the bilayer effect. Taken from: [24]

Figure 2.2: Illustrations of the bilayer waveguide

Here ρ is the radius of curvature, $\epsilon = (l_2 - l_1)/l_o$ the strain mismatch where l_1 and l_2 are the unstrained lengths and $l_o$is the , $d = d_1 + d_2$ the combined thickness, $n = E_1/E_2$ the ratio of the Young's Modulus for the two materials and $m = d_1/d_2$ the ratio of the thicknesses. The subscripts 1 and 2 refers to respectively the upper and lower layers.[23]

From the expression for ϵ, it can be seen that the radius of curvature does not depend directly on the intrinsic strain in each layer, but rather on the strain mismatch. Thus, even if all parameters but ϵ in equation 2.3 are known, the strain in each layer can not be uniquely determined from the radius of curvature. Given that many material effects, such as the strain induced bandgap shift described by the Pikus-Bir Hamiltonian, depends directly on the local strain, this poses an additional challenge when modelling the behavior of the bilayer cantilever. This is further complicated by the fact that intrinsic stress does not depend only on the lattice mismatch between a thin film and the underlying substrate, but also on how the method of which the upper layer is deposited.

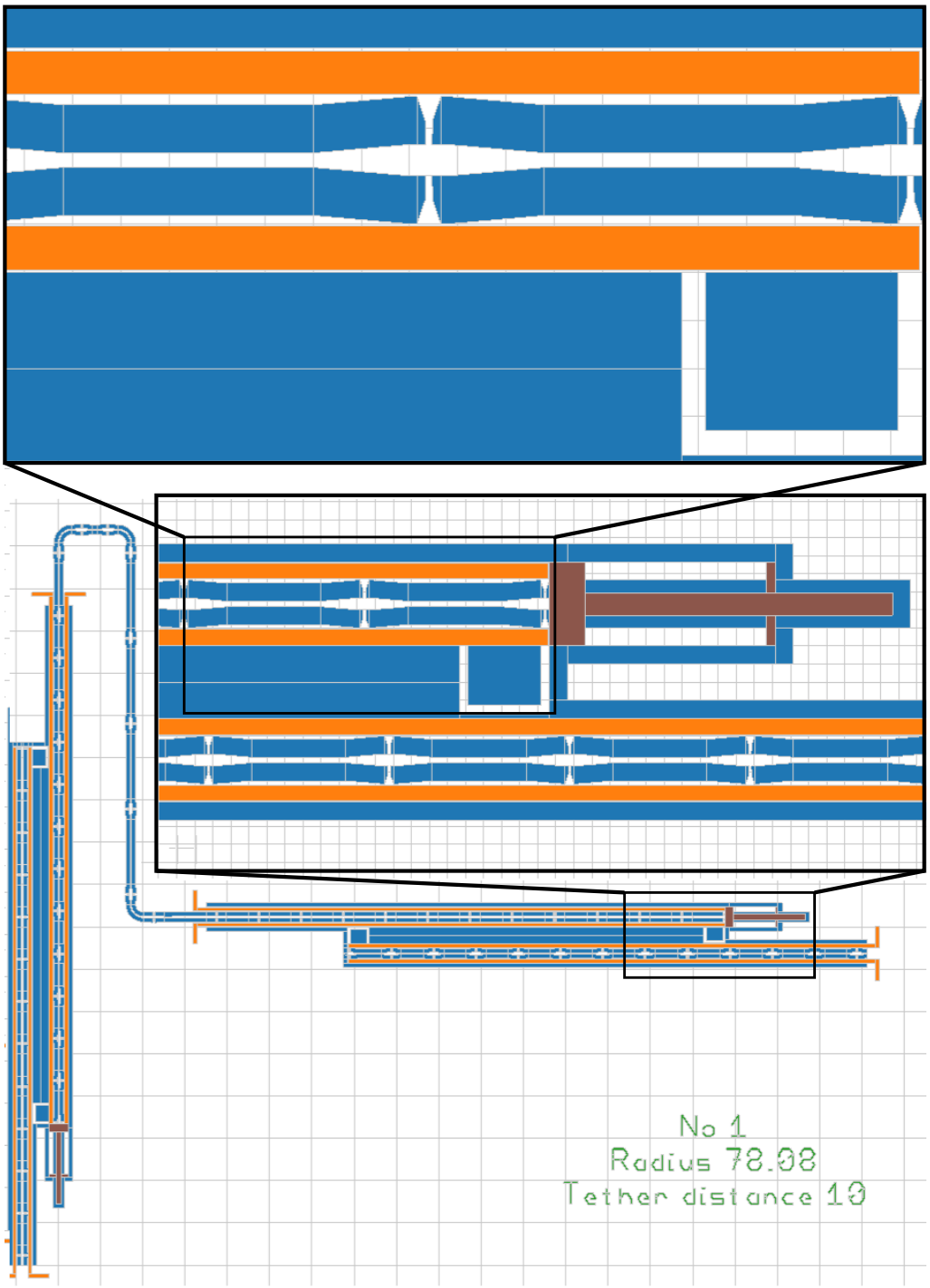

Figure 2.3: Illustrations of the bilayer waveguide mask. Here, the nickel strips are shown in orange, the GaAs suspended waveguides are shown in white, with the blue areas being the areas that will be etched away. The epoxy tip is shown in brown

By tailoring the length of the cantilever to $l = \pi\rho/2$, the bent waveguide can be fabricated to have the curvature of a quarter of a circle, resulting in the waveguide tip pointing straight up, allowing it to act as a coupler, with the tapered tips giving the large bandwidth and admitting TE and TM modes both, like on an in-plane tapered tip coupler, while having many of the advantages of etched gratings, such as being able to be placed anywhere on the chip and being accessible from the top window of a cryostate. The tip of the cantilever waveguide is capped by an epoxy cladding, giving a larger surface area.

The waveguides are stabilized using a hook technology, where two opposing cantilevers lock together, keeping the ends of both of them in a vertical position. One of the two locked-together cantilevers contains a tapered tip covered in an epoxy-cladding, allowing it to act as a coupler[33]. On figure 2.3 an illustration of the mask used to create the bilayer cantilever is shown. It can be seen how the waveguide consists of a narrow cantilever, connected to the Ni/GaAs bilayer cantilevers with tether bridges.

In this thesis, the transmittivity of this waveguide is characterized and analyzed. Understanding the behavior of strongly strained material requires a strong foundation of the material physics of deformed crystals and how the warping of the crystal lattice influences the optical, electrical and electronic properties of the material. In the next chapter, the necessary solid mechanics will be introduced, and condensed-matter physics based theories of strained materials will be laid out.

Chapter 3

Solid Mechanics and Quantum Materials Physics

Macroscopic and microscopic materials physics are intrinsically deeply connected. The atomic and molecular crystalline structure of solid materials regulate the macroscopic material properties such as stiffness, relative electric permittivity and optical index of refraction. Conversely, the application of macroscopic mechanical or electrical forces can disturb or warp the crystal structure, changing the material properties. Deformations of semiconductors can distort the energy bands and change the band gap energy. The application of electric fields along certain directions of anisotropic materials induces tensile or compressive forces, causing the object to deform. Powerful applied electric fields changes the periodical structure of semiconductors, smearing the conduction band and allowing sub-bandgap excitation. Any change in bandgap or absorption changes the optical properties of the material, and thus its abilities at conducting or guiding light. All of these phenomena interact, causing complex emerging responses.

In this chapter, an overview of materials physics is given. Basic solid mechanics is introduced and the formalisms used for describing displacement-strain and stress-strain relationships in different coordinate systems are described. Following this, basic semiconductor physics is laid out, including the band structure formalism for GaAs. From this, various material physics phenomena is introduced. This includes the Pikus-Bir Hamiltonian which describes strain-induced energy band warping in a direct band semiconductor, the piezo-electric and flexoelectric effects which describe an electric field induced in a dielectric material by respectively a homogenous strain and a strain gradient. Finally, the Franz-Keldysh effect is introduced, where a strong applied electric field smears the conduction band, causing a non-zero below-band absorption coefficient.

3.1 Stress and strain on crystals

In order to be able to describe the influence of deformation on microscopical material properties, an understanding of the physics of deformation and forces is needed. In this section, the basics of solid mechanics for objects undergoing large displacements are laid out, providing the necessary background for working with strain-induced changes in material parameters.

3.1.1 Strain and deformations

In comparison to traditional Newtonian mechanics, where objects are modelled as point masses or ideal rigid objects, solid mechanics offers a mathematical framework which enables a description of objects that twist, stretch, or bend in response to internal or external forces. This is in short

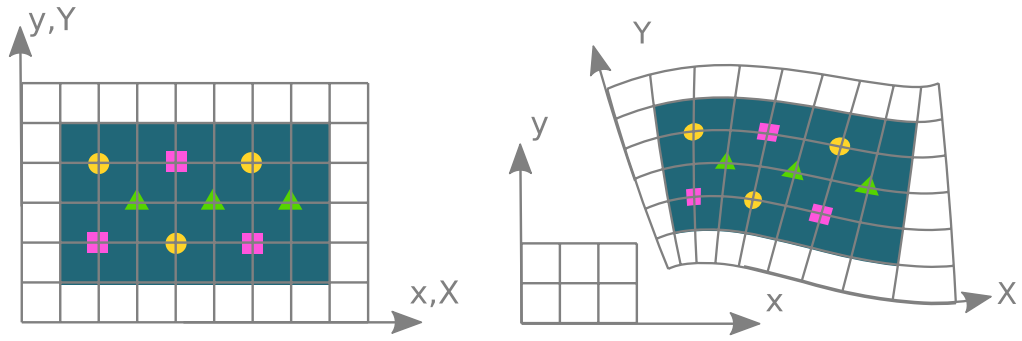

Figure 3.1: Material frame X,Y and spatial frame x,y before and after deformation

called deformations, which deals with displacement of an object with respect to itself, in contrast to translation and rotations, which describes the displacement of an object with respect to its surroundings.

For any displacement, no matter how large, a deformation gradient tensor F_{ij} can be defined. This deformation gradient tensor contains information about deformation and rotation, but not pure translation.[2]

$$F_{ij} = \frac{\partial x_i}{\partial X_j} = \frac{\partial u_i}{\partial X_j} + \delta_{ij} \tag{3.1}$$

Here x_i is the i'th component of the deformed position of the particle, X_i the i'th component of the original, undeformed position of the particle, and u_i the i'th component of the displacement vector, $u_i = x_i - X_i$. X_i, the original undeformed position, is considered unchanged for a material particle through its deformation. Thus, $\mathbf{X}$ can be considered a material coordinate system, which is fixed to the body, and is deformed with it. Meanwhile, x_i, describes the deformed configuration of the system, which changes with the position and configuration of the system. This makes $\mathbf{x}$ a spatial coordinate system, which is fixed in space. In figure 3.1, a comparison of a material and a spatial coordinate system is shown for an object undergoing a deformation. Before the deformation, the material and spatial system overlap. After the deformation, the material and spatial coordinate system differ. Note how the features of the object align with the same position in the material coordinate system both before and after deformation. The position of the object in the material coordinate system is constant, no matter what deformation the object undergoes.

Furthermore, the term $-\delta_{ij}$ ensures that translation is removed from the deformation gradient tensor.

The displacement vector, u_i, can be described using either spatial or material coordinates, and two intrinsically different mathematical formulations of continuum mechanics are reached depending on whether the updated spatial or the original material coordinates are used as the reference coordinates.

$$\mathbf{u}_{spatial}(\mathbf{x}) = \mathbf{x} - \mathbf{X}(\mathbf{x}), \qquad \mathbf{u}_{material}(\mathbf{X}) = \mathbf{x}(\mathbf{X}) - \mathbf{X} \tag{3.2}$$

When working with continuum mechanics, the goal is to define a quantity which describes the deformation of an object. Strain is used to describe this displacement of particles in a solid object relatively to the other particles in the same object. For small displacements, which also means that there can be at most a small rotation, the material coordinates and the spatial coordinates are approximately the same, and the two descriptions are thus also the same. From this, the Cauchy

strain tensor can be derived.

$$\epsilon_{ij} = \frac{1}{2}\left(F_{ij} + F_{ji}\right) - \delta_{ij} = \frac{1}{2}\left(\frac{\partial u_i}{\partial X_j} + \frac{\partial u_j}{\partial X_i}\right) \tag{3.3}$$

This description, however, breaks down for large displacements, meaning that the material coordinates can no longer be approximated to be identical to the spatial coordinates. Generally, the error on the Cauchy strain tensor is of the same order of magnitude as the deformation of the object relative to its dimensions.

For an object subjected to a large displacement, the strain must be defined in either material or spatial coordinates. Those two definitions are intrinsically different, and can not be regarded as mere coordinate transformations of each other. In this thesis, the material coordinates will be used exclusively, since this allows for easy extraction of stress and strain at the location of the various features in the undeformed structure.

From analysis of equation 3.3, it can be shown that an object undergoing rotation without deformation will have a non-zero Cauchy strain tensor, and thus it is necessary to find a tensor describing deformation without containing the rotation as well. [2] The Polar decomposition theorem states that any second order tensor (i.e. a matrix) with a positive determinant can be uniquely decompositioned into an orthogonal matrix, $\mathbf{R}\mathbf{R}^T = 1$ and a symmetric matrix $\mathbf{U} = \mathbf{U}^T$. Using this theorem the deformation tensor F can be decompositioned into an orthogonal tensor and a symmetric tensor

$$\mathbf{F} = \mathbf{R}\mathbf{U}. \tag{3.4}$$

It is known that a rotation matrix is always orthogonal. Furthermore, it can be shown that any tensor containing only displacement is always symmetrical. From the fact that the polar decomposition is unique, it is clear that in the polar decomposition of $\mathbf{F}$, $\mathbf{R}$ describes the rotation and $\mathbf{U}$ describes the deformation.

From this, it is possible to create a tensor containing only the displacement.

$$\mathbf{F}^T\mathbf{F} = (\mathbf{R}\mathbf{U})^T\mathbf{R}\mathbf{U} = \mathbf{U}^T\mathbf{R}^T\mathbf{R}\mathbf{U} = \mathbf{U}^2 = \mathbf{C} \tag{3.5}$$

The tensor $\mathbf{C}$ is called the right Cauchy-Green deformation tensor. From this, a material description of the strain known as the Green-Lagrange strain can be found[2]

$$\epsilon = \frac{1}{2}\left(\mathbf{C} - \mathbf{I}\right), \quad \epsilon_{ij} = \frac{1}{2}\left(\frac{\partial u_i}{\partial X_j} + \frac{\partial u_j}{\partial X_i} + \sum_k \frac{\partial u_k}{\partial X_i}\frac{\partial u_k}{\partial X_j}\right). \tag{3.6}$$

It is important to note that this non-linear strain-displacement relationship containing a second-order term is not a second order approximation, but is a complete description.

If the polar decomposition of $\mathbf{F}$ is done with the rotation matrix to the right, and the deformation matrix to the left, a spatial description known as the Almansi strain can be derived,

$$\mathbf{F} = \mathbf{V}\mathbf{R}, \quad \mathbf{F}\mathbf{F}^T = \mathbf{V}\mathbf{R}\mathbf{R}^T\mathbf{V}^T = \mathbf{V}^2 = \mathbf{B}. \tag{3.7}$$

$$\epsilon = \frac{1}{2}\left(\mathbf{I} - \mathbf{B}^{-1}\right), \quad \epsilon_{ij} = \frac{1}{2}\left(\frac{\partial u_i}{\partial x_j} + \frac{\partial u_j}{\partial x_i} - \sum_k \frac{\partial u_k}{\partial x_i}\frac{\partial u_k}{\partial x_j}\right) \tag{3.8}$$

By comparing equations 3.3, 3.6 and 3.8, it can be seen that the Cauchy strain tensor functions as a first order approximation of both the Green-Lagrange strain and the Almansi strain under the assumption that the material coordinate system can be approximated as the same.

3.1.2 Stress and forces

The purpose of solid mechanics is to create a mathematical framework capable of describing the relationship between material deformation, or strain, and the applied forces, or stress. Like strain, stress is a second order tensor, which is symmetrical for any object at rest [17]

$$\sigma = \begin{bmatrix} \sigma_{xx} & \sigma_{xy} & \sigma_{xz} \\ \sigma_{yx} & \sigma_{yy} & \sigma_{yz} \\ \sigma_{zx} & \sigma_{zy} & \sigma_{zz} \end{bmatrix}. \tag{3.9}$$

Since solid mechanics is used for very different materials, ranging from soft polymers to brittle crystals, different models are used to describe the relationship between stress and strain, depending on the materials involved and the type and magnitude of forces and deformations. In the case of small deformations (where the limit for what constitutes as "small" is highly material dependent) it is often possible to describe the force-displacement relationship linearly, which is known as Hooke's law. This is a law of linear elasticity where it's assumed that the stress-strain relationship is linear, and that it is elastic, meaning that the deformation is reversible rather than permanent.

In an isotropic crystal only two parameters are needed to describe the elastic properties of the material, which are Young's Modulus and Poisson's Ratio, which describe respectively the stiffness and incompressibility of a material.[17]. Young's modulus describes the materials ability to withstand change in length while being exposed to a tensile or compressive force along the same direction. Young's modulus is typically measured in Gigapascals. Meanwhile, Poisson's ratio describes the materials tendency to expand (contract) in directions perpendicular applied compressive (tensile) stress. For natural materials Poisson's ratio is between 0 and 0.5, while metamaterials with Poisson's ratio less than 0 have been engineered[14]. A perfectly incompressible material would have a Poisson's ratio of 0.5, describing how the material keeps its volume constant under uniaxial tension or compression by contracting or expanding in the directions perpendicular to the applied force.

However, for materials which do not consist of simple cubic crystals, this description is not sufficient. Nickel is a face-centered cubic lattice and GaAs is zincblende, meaning that it consists of two interwoven face-centered cubic lattices, one of gallium with base at $(0, 0, 0)$ and one of arsenide with base at $\left(\frac{1}{4}, \frac{1}{4}, \frac{1}{4}\right)$. Such materials have a degree of anisotropy or preferred directions, which for Gallium Arsenide is examplified in its cleavage axis [110]. In order to describe the force-deformation relationship containing anisotropy, more than two parameters are needed.

For any elastic material, the relation between stress and strain can be described using the compliance tensor S and the stiffness tensor C, which are each other's inverse.

$$\sigma = C\epsilon, \quad \epsilon = S\sigma \tag{3.10}$$

Since both σ and ϵ are second-rank tensors, the compliance tensor S and stiffness tensor C connecting them both are fourth-rank tensors. While it might seem like this formalism is very complicated, with 81 components, it can be simplified greatly by exploiting symmetries.

As mentioned, the stress tensor is symmetrical for any object at rest. Furthermore, it can trivially be seen from equations 3.3 and 3.6 that the strain tensor is intrinsically symmetrical. This enables the use of so-called Voigt notation, in which the indices of the stress and strain tensors are made into vectors with 6 indices, allowing the compliance and stiffness tensor to be described as 6x6 second rank tensors. [32]

This makes the stiffness and compliance matrices into 6×6 matrices, which are symmetric as a consequence of the strain and stress tensors being symmetric, meaning that any elastic material, no matter how anisotropic, can have 21 constants at most describing Hooke's law.[17]

[i]Figure from `https://doc.comsol.com/5.5/doc/com.comsol.help.sme/sme_ug_theory.06.04.html`

$$\boldsymbol{\sigma} = \begin{bmatrix} \sigma_{xx} & \sigma_{xy} & \sigma_{xz} \\ & \sigma_{yy} & \sigma_{yz} \\ & & \sigma_{zz} \end{bmatrix}$$

Figure 3.2: Order of indices in the relabelled Voigt notation [i]

The number of non-zero components in the compliance and stiffness matrices is highly material dependent. For Nickel and Gallium Arsenide, which both are cubic face-centered lattices, the matrices have only 3 independent non-zero components. With the [100], [010] and [001] directions as the bases, the compliance matrix is as follows [32]

$$\begin{bmatrix} \epsilon_{xx} \\ \epsilon_{yy} \\ \epsilon_{zz} \\ 2\epsilon_{yz} \\ 2\epsilon_{xz} \\ 2\epsilon_{xy} \end{bmatrix} = \begin{bmatrix} S_{11} & S_{12} & S_{12} & 0 & 0 & 0 \\ S_{12} & S_{11} & S_{12} & 0 & 0 & 0 \\ S_{12} & S_{12} & S_{11} & 0 & 0 & 0 \\ 0 & 0 & 0 & S_{44} & 0 & 0 \\ 0 & 0 & 0 & 0 & S_{44} & 0 \\ 0 & 0 & 0 & 0 & 0 & S_{44} \end{bmatrix} \begin{bmatrix} \sigma_{xx} \\ \sigma_{yy} \\ \sigma_{zz} \\ \sigma_{yz} \\ \sigma_{xz} \\ \sigma_{xy} \end{bmatrix} \tag{3.11}$$

Conversely, the stiffness matrix is

$$\begin{bmatrix} \sigma_{xx} \\ \sigma_{yy} \\ \sigma_{zz} \\ \sigma_{yz} \\ \sigma_{xz} \\ \sigma_{xy} \end{bmatrix} = \begin{bmatrix} C_{11} & C_{12} & C_{12} & 0 & 0 & 0 \\ C_{12} & C_{11} & C_{12} & 0 & 0 & 0 \\ C_{12} & C_{12} & C_{11} & 0 & 0 & 0 \\ 0 & 0 & 0 & C_{44} & 0 & 0 \\ 0 & 0 & 0 & 0 & C_{44} & 0 \\ 0 & 0 & 0 & 0 & 0 & C_{44} \end{bmatrix} \begin{bmatrix} \epsilon_{xx} \\ \epsilon_{yy} \\ \epsilon_{zz} \\ 2\epsilon_{yz} \\ 2\epsilon_{xz} \\ 2\epsilon_{xy} \end{bmatrix}. \tag{3.12}$$

Note how in the Voigt notation, the shear strain terms are multiplied by 2. This is a common convention, and results from a common engineering definition of the shear strain term being

$$\gamma_{ij} = 2\epsilon_{ij}. \tag{3.13}$$

Many elastic parameters are defined using γ_{ij} rather than ϵ_{ij}. One can choose whether to use $\gamma_{ij} = 2\epsilon_{ij}$ or ϵ_{ij} in the Voigt notation, as long as the use is kept consistent and the material parameters are adjusted accordingly. However, for strains on 3×3 tensor from, ϵ_{ij} must be used for the shear terms because otherwise the results will not be consistent under rotation of the coordinate system. In this thesis, the notation $2\epsilon_{ij}$ was chosen, in order to allow using the same material parameters as in most of the available literature, while also keeping the relationship between the shear strains in respectively the Voigt notation and the 3×3 tensor notation explicit.

In isotropic crystals, there isn't any characteristic directions. The compliance and stiffness matrices of isotropic cubic crystals only have two independent components, with

$$C_{44} = \frac{C_{11} - C_{22}}{2}. \tag{3.14}$$

Meanwhile, the anisotropy of a cubic crystal can be described as

$$A = \frac{2C_{44}}{C_{11} - C_{22}}. \tag{3.15}$$

For GaAs, $C_{11} = 11.88 \cdot 10^{10}$ N/m^2, $C_{12} = 5.34 \cdot 10^{10}$ N/m^2, $C_{44} = 5.94 \cdot 10^{10}$ N/m^2[11]. The anisotropy of GaAs is thus

$$A = \frac{2 \cdot 5.94 \cdot 10^{10} \text{ N/m}^2}{11.88 \cdot 10^{10} \text{ N/m}^2 - 5.34 \cdot 10^{10} \text{ N/m}^2} = 1.81. \tag{3.16}$$

3.2 Semiconductor physics and light-matter interaction

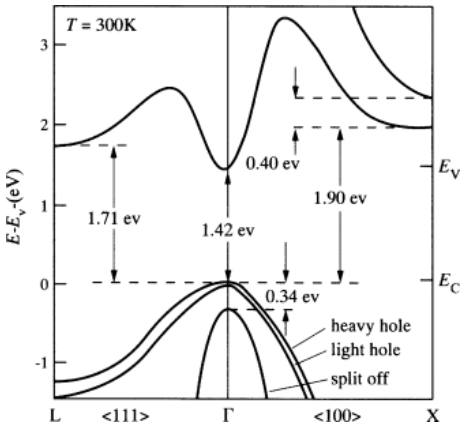

(a) Band structure for Gallium Arsenide. Figure from [29]

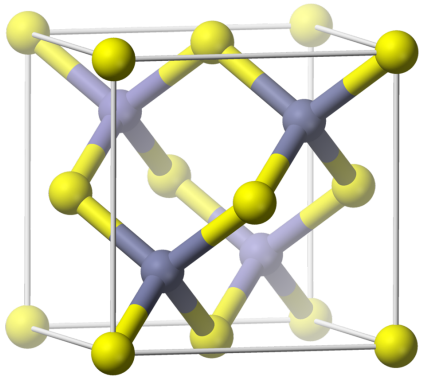

(b) Zincblende crystal structure, which GaAs has. Figure from[5]

Figure 3.3: Band-gap and crystal structure for GaAs, a direct bandgap semiconductor with a zincblende crystal structure.

In a crystalline material, the potential in the Schrödinger equation is periodic and determined by the crystal structure of the material, such that [32]

$$\left(-\frac{\hbar^2}{2m}\nabla^2 + V(\mathbf{r})\right)\psi(\mathbf{r}) = E\psi(\mathbf{r}). \tag{3.17}$$

In the nearly-free electron model, the allowed energy levels are found by solving the Schrödinger's Equation for electrons who are very loosely bound to the crystal lattice. Due to the periodicity of the crystal lattice, the Bloch theorem holds, and the wave functions can be shown to be those of a free electron modulated by a function with the same periodicity as the crystal lattice.

$$\psi_{\mathbf{k}}(\mathbf{r}) = u_{\mathbf{k}}(\mathbf{r})e^{i\mathbf{k}\cdot\mathbf{r}}. \tag{3.18}$$

Here $e^{i\mathbf{k}\cdot\mathbf{r}}$ is a plane wave with a wave vector $\mathbf{k}$, and $u_{\mathbf{k}}(\mathbf{r}) = u_{\mathbf{k}}(\mathbf{r}+\mathbf{R})$ is s periodic modulating function where $\mathbf{R}$ is a translation vector with the same periodicity as the crystal, $\mathbf{R} = n\mathbf{a}_x + m\mathbf{a}_y + l\mathbf{a}_z$, where n, m and l are integers.

By solving the Schrödinger equation for this system, the allowed energies for the k-vector can be found. Due to the symmetry of the crystal lattice and the periodicity of the modulating function any solution for $\mathbf{k}' = \mathbf{k} \pm 2\pi/\mathbf{R}$ is also a solution for $\mathbf{k}$. Thus the solutions can be folded into a single Brillouin Zone spanding the reciprocal lattice of a single unit cell.[30]

As can be seen in figure 3.3a, the allowed energies take form of so-called discrete energy bands, which are separated by band gaps. These energy bands are occupied by the electrons in the

[i]Figure from `https://www.sciencedirect.com/science/article/pii/B0080431526006124`

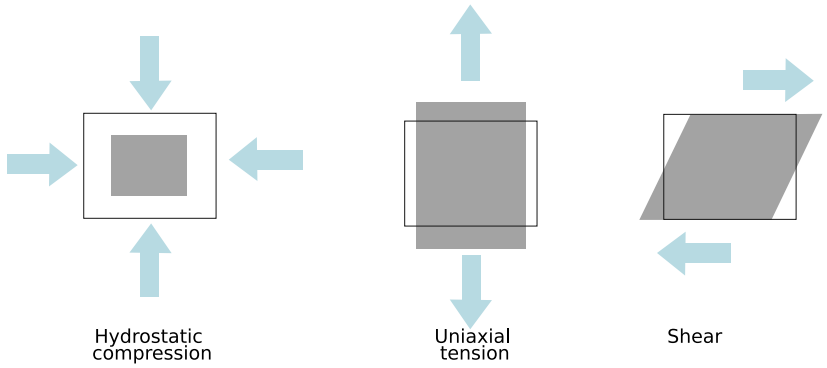

Figure 3.4: Illustration of three different types of stress on a 2-dimensional object. Note how the object being subjected to uniaxial tensile stress contracts in the direction perpendicular to the application of the stress, shown by pale blue arrows.

crystal. In GaAs, which is a semiconductor, the so-called valence bands are completely filled while the conduction band is empty, making electrical conduction impossible. However, the band gap of GaAs is relatively small at $E_g = 1.42\,\text{eV}$ at room temperature, and an incoming photon with $E > E_g$ is capable of exciting an electron from one of the valence bands to the conduction band. This creates an exciton, or an electron hole pair, an electrically neutral quasiparticle consisting of the bound state between an electron in the conduction band and a hole, or absence of electron, in the valence band.

For GaAs, which is a zincblende crystal whose crystal structure can be seen in figure 3.3b, the valence band is triply degenerate at the Γ point (six times counting electron spin), which is the center of the crystal and the point containing the band gap. Due to spin-orbit interactions, one of the bands gains a split-off energy of 0.34 eV. The two remaining bands are termed the light-hole (LH) band and the heavy-hole (HH) band. While they are degenerate at the Γ point, their dispersion relations $E(\mathbf{k})$ differs for $\mathbf{k} \neq 0$.[32]

In the effective mass model of modelling dispersion, the bands can be modelled as parabolas close to the zone center. In this model, the electrons are modelled with the same formulas as in free space, but the mass of the electron, $m_0 = 9.11 \cdot 10^{-31}$ kg is replaced with an effective mass. For GaAs, the effective mass for the light holes is $m_{LH} = 0.082\,m_0$ and the effective mass for the heavy holes is $m_{HH} = 0.45\,m_0$.

3.3 Strain in crystals and the Pikus-Bir Hamiltonian

An arbitrary strain tensor can be decomposed into three separate tensors, each corresponding to a respective type of strain.

$$\begin{pmatrix} \epsilon_{xx} & \epsilon_{xy} & \epsilon_{xz} \\ \epsilon_{yx} & \epsilon_{yy} & \epsilon_{yz} \\ \epsilon_{zx} & \epsilon_{zy} & \epsilon_{zz} \end{pmatrix} = \frac{1}{3}(\epsilon_{xx} + \epsilon_{yy} + \epsilon_{zz}) \begin{pmatrix} 1 & 0 & 0 \\ 0 & 1 & 0 \\ 0 & 0 & 1 \end{pmatrix} + \begin{pmatrix} 0 & \epsilon_{xy} & \epsilon_{xz} \\ \epsilon_{yx} & 0 & \epsilon_{yz} \\ \epsilon_{zx} & \epsilon_{zy} & 0 \end{pmatrix} \tag{3.19}$$

$$+ \frac{1}{3} \begin{pmatrix} 2\epsilon_{xx} - (\epsilon_{yy} + \epsilon_{zz}) & 0 & 0 \\ 0 & 2\epsilon_{yy} - (\epsilon_{xx} + \epsilon_{zz}) & 0 \\ 0 & 0 & 2\epsilon_{zz} - (\epsilon_{yy} + \epsilon_{zz}) \end{pmatrix} \tag{3.20}$$

Here, the first matrix corresponds to hydrostatic strain, or strain causing a change in volume while keeping all proportions and angles constant. The second matrix corresponds to the shear

strain, meaning any strain that cause a deformation along the local axes. The third matrix corresponds to non-hydrostatic normal strain, meaning strain that is applied along directions perpendicular to the faces. This strain will change lengths with respect to each other while keeping all angles in the local coordinate system constant.

An illustration of the different types of stress and strain can be seen in figure 3.4. Here the hydrostatic compressive stress corresponds to the first matrix, the shear stress corresponds to the second matrix, and the uniaxial tensile stress corresponds to the third matrix.

Applied strain will distort the crystal structure, breaking symmetry or changing the periodicity of the material. Applying ordinary perturbative methods to describe the energy band shifts caused by the change in the crystal is usually not sufficient, due to two reasons[32]. Firstly, even with a small change of lattice periodicity, the displacement of atoms away from the chosen origo will over a mesoscopic sample easily be of the same order of magnitude as the lattice periodicity. This means that the perturbation to the potential, $V_0(\mathbf{x}) - V(\mathbf{x})$, is not necessarily small. Secondly, the deformation changes the periodicity of the crystal, meaning that the old set of Bloch functions are no longer sufficient to describe the system. In the Pikus-Bir formalism, this is dealt with by carrying out a coordinate transform where the deformed coordinates are described as a function of the undeformed coordinates. In this coordinate transformation, the deformed and the undeformed configurations have the same boundary conditions. From here, the Pikus-Bir perturbative method of finding the energy band shifts as a function of the strain can be found.

The energy bands are an emergent property in a macroscopic crystal caused by the crystal structure. While hydrostatic strain keeps any symmetry inherent in the crystal, both shear and uni- or bi-axial normal strain will break up different types of symmetries. Since degeneracies in semiconductor energy bands arise due to symmetries of the crystal structure, lifting any symmetry will also lift the corresponding degeneracies. In GaAs, the conduction band, which has its minimum at the Γ point, is non-degenerate, and strain-induced energy shift is caused by hydrostatic strain only. This strain can be described by the deformation potential

$$a_c = \frac{dE_c}{d\,\mathrm{ln}V} \tag{3.21}$$

Here $d\,\mathrm{ln}V$ is the relative crystal volume change

$$d\,\mathrm{ln}V = \frac{dV}{V} = \mathrm{Tr}(\epsilon) = \epsilon_{xx} + \epsilon_{yy} + \epsilon_{zz} \tag{3.22}$$

This means that for small volume changes, the shift of the conduction band is

$$E_c = a_c \mathrm{Tr}(\epsilon) \tag{3.23}$$

The valence band of a cubic semiconductor has three times degeneracy at the Γ point (six times if electron spin is counted) because the x, y, and z directions are the same [32]. In GaAs, which is a zincblende semiconductor, the valence is only doubly degenerate with a heavy hole and a light hole band, while the third band - the split-off band - has split off. This degeneracy at the Γ point means that not only will hydrostatic strain cause the energy levels to shift as described by a valence band degeneration potential,

$$a_v = \frac{dE_v}{d\,\mathrm{ln}V}, \tag{3.24}$$

but also any non-hydrostatic strain will destroy the crystal symmetry, splitting the heavy and light holes while potentially also causing mixing of the heavy hole and light hole eigenstates.

The Pikus-Bir Hamiltonian for describing the band gap shifts at the Γ point caused by strain in GaAs is the following[32]

$$H = \begin{pmatrix} -P_\epsilon - Q_\epsilon & S_\epsilon & -R_\epsilon & 0 & \frac{1}{\sqrt{2}S_\epsilon} & \sqrt{2}R_\epsilon \\ S_\epsilon^* & -P_\epsilon + Q_\epsilon & 0 & -R_\epsilon & \sqrt{2}Q_\epsilon & -\sqrt{\frac{3}{2}}S_\epsilon \\ -R_\epsilon^* & 0 & -P_\epsilon + Q_\epsilon & -S_\epsilon & -\sqrt{\frac{3}{2}}S_\epsilon^* & -\sqrt{2}Q_\epsilon \\ 0 & -R_\epsilon^* & -S_\epsilon^* & -P_\epsilon - Q_\epsilon & \sqrt{2}R_\epsilon^* & 0 \\ \frac{1}{\sqrt{2}} & \sqrt{2}Q_\epsilon & -\sqrt{\frac{3}{2}}S_\epsilon & \sqrt{2}R_\epsilon & -P_\epsilon - \Delta & 0 \\ -\sqrt{2}R_\epsilon^* & -\sqrt{\frac{3}{2}}S_\epsilon^* & -\sqrt{2}Q_\epsilon & \frac{1}{\sqrt{2}}S_\epsilon & 0 & -P_\epsilon - \Delta \end{pmatrix} \begin{matrix} |HH\uparrow\rangle \\ |LH\uparrow\rangle \\ |LH\downarrow\rangle \\ |HH\downarrow\rangle \\ |SO\uparrow\rangle \\ |SO\downarrow\rangle \end{matrix}. \tag{3.25}$$

With

$$\begin{aligned} P_\epsilon &= a_v(\epsilon_{xx} + \epsilon_{yy} - \epsilon_{zz}), \qquad Q_\epsilon = -\frac{b}{2}(\epsilon_{xx} + \epsilon_{yy} - 2\epsilon_{zz}) \\ R_\epsilon &= \frac{\sqrt{3}}{2}b(\epsilon_{xx} - \epsilon_{yy}) - id\epsilon_{xy}, \quad S_\epsilon = -d(\epsilon_{xz} - i\epsilon_{yz}) \end{aligned} \tag{3.26}$$

Here a_v is the hydrostatic deformation potential for the valence band, b and d the shear deformation potential for the valence band, and Δ the energy splitting caused by the spin-orbit interaction. For GaAs $\Delta = 0.34\,\text{eV}$, $a_c = -7.17\,\text{eV}$, $a_v = -1.16\,\text{eV}$, $b = -2\,\text{eV}$, $d = -4.8\,\text{eV}$[32].

As a toy example, for equibiaxial strain on the [001] axis, $\epsilon_{xx} = \epsilon_{yy}$ and $\epsilon_{xy} = \epsilon_{yz} = \epsilon_{zx} = 0$. This gives $R_\epsilon = 0$ and $S_\epsilon = 0$, resulting in.

$$\begin{aligned} E_{v,hh} &= -P_\epsilon - Q_\epsilon \\ E_{v,lh} &= -P_\epsilon + \tfrac{1}{2}\left(Q_\epsilon - \Delta + \sqrt{\Delta^2 + 2\Delta Q_\epsilon + 9Q_\epsilon^2}\right) \\ E_{v,so} &= -P_\epsilon + \tfrac{1}{2}\left(Q_\epsilon - \Delta - \sqrt{\Delta^2 + 2\Delta Q_\epsilon + 9Q_\epsilon^2}\right) \end{aligned} \tag{3.27}$$

3.3.1 Simplified 4x4 Pikus-Bir Hamiltonian.

If the split-off bands are disregarded, which is possible whenever the energy band gap shift caused by strain is much smaller than the split-off energy Δ, the 6-band Pikus-Bir Hamiltonian can be simplified to a 4-band model, which can be used for calculating the energy shifts of the heavy hole and light hole bands (or the hybridizations thereof) while neglecting the influence from the split-off band. Using this 4×4 Pikus-Bir Hamiltonian, the two sets of Eigenvalues, each of which are doubly degenerate, can be calculated analytically[32]

$$H = \begin{pmatrix} -P_\epsilon - Q_\epsilon & S_\epsilon & -R_\epsilon & 0 \\ S_\epsilon^* & -P_\epsilon + Q_\epsilon & 0 & -R_\epsilon \\ -R_\epsilon^* & 0 & -P_\epsilon + Q_\epsilon & -S_\epsilon \\ 0 & -R_\epsilon^* & -S_\epsilon^* & -P_\epsilon - Q_\epsilon \end{pmatrix} \begin{matrix} |HH\uparrow\rangle \\ |LH\uparrow\rangle \\ |LH\downarrow\rangle \\ |HH\downarrow\rangle \end{matrix}. \tag{3.28}$$

It can clearly be seen from the non-zero diagonal elements of equations 3.25 and 3.28 that strain will cause coupling between the light hole and the heavy hole bands unless $R_\epsilon = 0$, $S_\epsilon = 0$. From equation 3.26 it can be seen that this is the case when $\epsilon_{xx} = \epsilon_{yy}$ and $\epsilon_{yz} = \epsilon_{xy} = \epsilon_{zx} = 0$, meaning that the strain must be either biaxial or hydrostatic. Using this 4×4 Pikus-Bir Hamiltonian, the two sets of Eigenvalues, each of which are doubly degenerate, can be calculated analytically[32]

$$E_{1,2} = -P_\epsilon \mp \sqrt{|Q_\epsilon|^2 + |R_\epsilon|^2 + |S_\epsilon|^2} \tag{3.29}$$

Here the bands are referred as band 1 and 2, in order to make it clear that they are not necessarily the HH and LH bands, but hybridizations of them.

This gives a splitting of the valence bands

$$\Delta E = 2\sqrt{|Q_\epsilon|^2 + |R_\epsilon|^2 + |S_\epsilon|^2}. \tag{3.30}$$

Combined with

$$E_c = a_c(\epsilon_{xx} + \epsilon_{yy} + \epsilon_{zz}) \tag{3.31}$$

$$P = a_v(\epsilon_{xx} + \epsilon_{yy} + \epsilon_{zz}) \tag{3.32}$$

The total energy shift can be written up as

$$\Delta E_{1/2} = E_c - E_{1/2} = (a_c + a_v)\,\mathrm{eV}(\epsilon_{xx} + \epsilon_{yy} + \epsilon_{zz}) \mp \sqrt{|Q_\epsilon|^2 + |R_\epsilon|^2 + |S_\epsilon|^2} \tag{3.33}$$

For an easier understanding, the total energy change can be considered to be two separate effects, one inducing a shift of the overall energy state, and one splitting the energies.

$$E_{shift} = (a_c + a_v)\,\mathrm{eV}(\mathrm{Tr}(\epsilon)), \quad E_{split} = \sqrt{|Q_\epsilon|^2 + |R_\epsilon|^2 + |S_\epsilon|^2} \tag{3.34}$$

For biaxial strain with no shear strain, the HH and LH bands are

$$E_{HH} = -P_\epsilon - Q_\epsilon, \quad E_{LH} = -P_\epsilon + Q_\epsilon \tag{3.35}$$

Hydrostatic compressive strain thus gives both E_1 and E_2 a positive shift, while tensile stress gives them a negative shift. Furthermore, the states are split by an amount decided by the non-hydrostatic strain described by Q_ϵ, R_ϵ and S_ϵ. In these calculations, E_1 is the lower state while E_2 is the upper state. For non-zero R_ϵ and S_ϵ, the states are a superposition of the LH and HH states while for $R_\epsilon = S_\epsilon = 0$, E_1 is HH for $Q_\epsilon > 0$ and LH for $Q_\epsilon < 0$, while E_2 is HH for $Q_\epsilon < 0$ and LH for $Q_\epsilon > 0$. For small values of R and S, the $E_{1/2}$ values can be regarded as being approximately either HH or LH, with the exact allocation depending on the sign of Q.

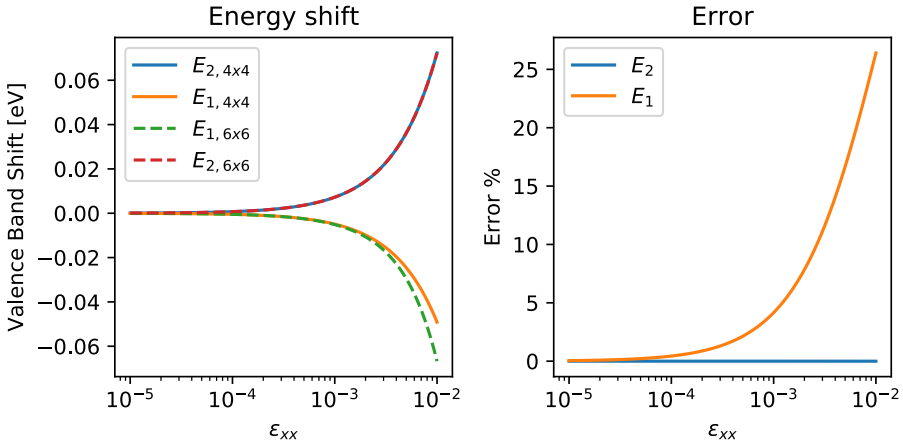

Figure 3.5: Error due to neglecting split-off effect for biaxial strain with shear strain. $\epsilon_{xx} = \epsilon_{yy} = -\epsilon_{zz} = \frac{1}{1.1}\epsilon_{xy}, \epsilon_{yz} = \epsilon_{zx} = 0$

Figure 3.5 shows the error calculating the valence band shifts using the 4×4 Hamiltonian, which is solved analytically, compared to the 6×6 Hamiltonian, which must be solved numerically. It can clearly be seen how the error on the 4×4 Hamiltonian is very small for small strains, and then becomes rapidly higher as the strain grows.

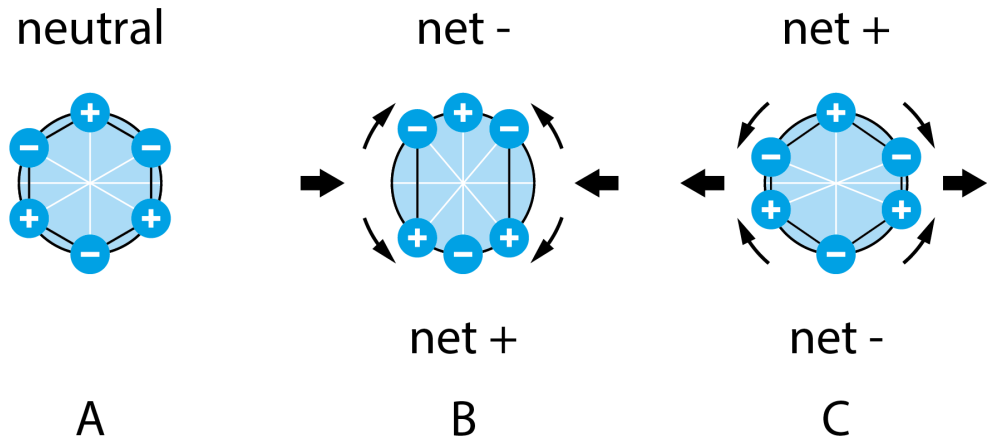

Figure 3.6: Demonstration of Piezoelectric effect. Figure taken from [8]

Materials subjected to large strains, especially when shear strain terms are involved, shows complex and fascinating behavior with regard to their electric, optical and electronic properties. Using tight-binding theory, LH and HH modes describe different combinations of angular momentum orbitals in semiconductor valence bands. The spin-orbit interaction causes the valence band to split into LH, HH and SO bands, with the heavy holes have the quantum number $j = 3/2, m = \pm 3/2$, while the light holes have the quantum number $j = 3/2, m = \pm 1/2$. Using tight-binding theory, it can be shown that both the LH states and the HH states consist of p-type orbitals[36]. Which p-type orbitals they consist of depends of the orientation of the quantization axis. The HH state consists of a combination of orbitals perpendicular to the quantization axis, giving it a doughnut-like shape. Conversely, the LH state consists of the p-orbital parallel to the quantization axis, giving it a dumbbell-like shape. In quantum dots, the optical selection rules are usually strongly dependent on the orientation of the natural quantization axis, which is often parallel to the growth direction [36]. Epitaxically grown quantum dots are often strongly confined in the vertical direction, making the natural quantization axis is the z-axis, meaning that the hole states become HH_z and LH_z. Combining with the s-type nature of the electron Bloch function, the doughnut shaped HH_z will only couple to photons with the electric field perpendicular to the z-axis, which for light propagating in a waveguide lying in the x-y plane is the TE mode. Similarly, the LH_z state is dumbbell shaped along the z-axis, and will couple to the TM mode.

3.4 Piezoelectricity

Piezoelectricity is an property found in some materials, in which application of strain along certain axes will lead to an induced electric polarization. Conversely, the reverse piezoelectric effect is when application of an electric potential will lead to a stress across the axes.

The piezoelectric effect is found in crystals that lack a center of inversion. The center of inversion is a feature of highly symmetric crystals, and means that at each point (x,y,z) which has a atom, the opposite point(-x,-y,-z), measured with the center of inversion as the origo, has an identical copy of the same atom[32].

Intuitively, the piezoelectric effect can be understood as a deformation of the crystal causing an electrical polarization, as can be seen in figure 3.6. The constitutive equations describing the piezoelectric effect takes different forms depending on whether respectively the stress or strain and

[i] https://www.biolinscientific.com/blog/what-is-piezoelectricity

the applied electric field or the electric displacement field are used as the dependent variables.

$$\begin{aligned} \epsilon &= \mathbf{S}\cdot\sigma + \mathbf{d}^T\cdot\mathbf{E} \qquad & \sigma &= \mathbf{C}\cdot\epsilon - \mathbf{e}^T\cdot\mathbf{E} \\ \mathbf{D} &= \mathbf{d}\cdot\sigma + \varepsilon\cdot\mathbf{E} & \mathbf{D} &= \mathbf{e}\cdot\epsilon + \varepsilon\cdot\mathbf{E}. \end{aligned} \tag{3.36}$$

To the left, the constitutive equations are shown on strain-charge form, and to the right stress-charge form, where the name comes from the two quantities on the left side of the equations[9]. As before, ϵ and σ are strain and stress written as a 6×1 vector using Voigt notation, $\mathbf{S}$ and $\mathbf{C}$ the compliance and stiffness tensors describing the stress-strain relationship for elastic deformations. The tensors $\mathbf{d}$ and $\mathbf{e}$ contain the piezoelectric coupling constants for respectively the stress-charge and the strain-charge forms.

Furthermore, $\mathbf{D}$ and $\mathbf{E}$ are the electric polarization field and the electric field, which are related by $\mathbf{D}_{non\_piezo} = \varepsilon_0\mathbf{E} + \mathbf{P}$. Here is $\varepsilon = \varepsilon_r\varepsilon_0 = \varepsilon_0(1+\chi)$, and $\varepsilon\mathbf{E} = \varepsilon_0\mathbf{E} + \mathbf{P}$.

It is also possible to write up strain-voltage and stress-voltage forms containing $\mathbf{E}$ on the left side of the equation, but they will not be used here.

Given that the strain is a second order tensor, and that the electric field is a first order tensor, or a vectorial quantity, a third order tensor is needed to connect them. However, with the use of Voigt notation $\mathbf{d}$ and $\mathbf{e}$ reduces to second order tensors, which can be represented as matrices.

With no stress and strain other than what results from the piezo-electric effect, the constitutive equations for the direct piezo-electric effect reduces to

$$\epsilon_i = \sum_j d_{ij}E_j, \quad \sigma_i = \sum_j -e_{ij}E_j. \tag{3.37}$$

Similarly, in the case of no external applied field, the polarization induced from applied stress or strain by the reverse piezoelectric effect is

$$P_i = \sum_j d_{ij}\sigma_j \quad P_i = \sum_j e_{ij}\epsilon_j. \tag{3.38}$$

Gallium Arsenide, like other zincblende semiconductors, have a relatively high degree of symmetry, and has only a single non-zero tensor element in the piezoelectric coupling constants, $e_{14} = -0.16\ \mathrm{C/m^2}$, $d_{14} = -2.6\cdot 10^{-12}\ \mathrm{m/V}$ where $d_{14} = e_{14}S_{14}$ [32].With the three axes written up along the [100], [010] and [001] crystal axes, the reverse piezo-electric tensors on stress-charge and strain-charge form for Gallium Arsenide are

$$\begin{bmatrix}\epsilon_{xx}\\ \epsilon_{yy}\\ \epsilon_{zz}\\ 2\epsilon_{yz}\\ 2\epsilon_{zx}\\ 2\epsilon_{xy}\end{bmatrix} = \begin{bmatrix}0 & 0 & 0\\ 0 & 0 & 0\\ 0 & 0 & 0\\ d_{14} & 0 & 0\\ 0 & d_{14} & 0\\ 0 & 0 & d_{14}\end{bmatrix}\begin{bmatrix}\mathbf{E}_1\\ \mathbf{E}_2\\ \mathbf{E}_3\end{bmatrix}, \quad \begin{bmatrix}\sigma_{xx}\\ \sigma_{yy}\\ \sigma_{zz}\\ \sigma_{yz}\\ \sigma_{zx}\\ \sigma_{xy}\end{bmatrix} = -\begin{bmatrix}0 & 0 & 0\\ 0 & 0 & 0\\ 0 & 0 & 0\\ e_{14} & 0 & 0\\ 0 & e_{14} & 0\\ 0 & 0 & e_{14}\end{bmatrix}\begin{bmatrix}\mathbf{E}_1\\ \mathbf{E}_2\\ \mathbf{E}_3\end{bmatrix}. \tag{3.39}$$

For a toy example, if an electric field is applied along the $\mathbf{E}_3$ direction, it results in

$$\begin{bmatrix}\epsilon_{xx}\\ \epsilon_{yy}\\ \epsilon_{zz}\\ 2\epsilon_{yz}\\ 2\epsilon_{zx}\\ 2\epsilon_{xy}\end{bmatrix} = \begin{bmatrix}0 & 0 & 0\\ 0 & 0 & 0\\ 0 & 0 & 0\\ d_{14} & 0 & 0\\ 0 & d_{14} & 0\\ 0 & 0 & d_{14}\end{bmatrix}\begin{bmatrix}0\\ 0\\ \mathbf{E}_3\end{bmatrix} = \begin{bmatrix}0\\ 0\\ 0\\ 0\\ 0\\ 2d_{14}\mathbf{E}_3\end{bmatrix}. \tag{3.40}$$

This means that the only non-zero components of the strain tensor are $\sigma_{12} = \sigma_{21} = d_{14}\mathbf{E}_3$. Applying an electric field along one axis thus causes a shear strain along the crystal axes perpendicular to that direction.

For a cantilever cut along the [110],[$\bar{1}$10] and [001] directions, the strain along [110] and [$\bar{1}$10] caused by application of an electric field along [001] can be calculated by transforming the Voigt notation strain tensor back into a 3×3 strain tensor and rotating the coordinate system of the tensor by $-\pi/4$[31]

$$\begin{pmatrix} \frac{1}{\sqrt{2}} & -\frac{1}{\sqrt{2}} & 0 \\ \frac{1}{\sqrt{2}} & \frac{1}{\sqrt{2}} & 0 \\ 0 & 0 & 1 \end{pmatrix} \begin{pmatrix} 0 & d_{14}\mathbf{E} & 0 \\ d_{14}\mathbf{E} & 0 & 0 \\ 0 & 0 & 0 \end{pmatrix} \begin{pmatrix} \frac{1}{\sqrt{2}} & \frac{1}{\sqrt{2}} & 0 \\ -\frac{1}{\sqrt{2}} & \frac{1}{\sqrt{2}} & 0 \\ 0 & 0 & 1 \end{pmatrix} = \begin{pmatrix} -d_{14}\mathbf{E} & 0 & 0 \\ 0 & d_{14}\mathbf{E} & 0 \\ 0 & 0 & 0 \end{pmatrix}. \tag{3.41}$$

With the coordinate system of the strain tensor being rotated $-\pi/4$ radians along the [001] plane, the strain is now measured along the [110],[$\bar{1}$10] and [001] crystal directions. It can be seen that the current strain is biaxial along [110] and [$\bar{1}$10]

A positive electric potential applied on top of the dielectric cantilever will lead to a negative field inside the cantilever since $\mathbf{E} = -\nabla V$. In this case the negative signs of d_{14} and E_3 will cancel each other out, meaning that the cantilever will experience tensile strain along [$\bar{1}$10] and compressive strain along [110].

For a bilayer cantilever with a layer of nickel on top, the GaAs attempting to either expand or compress due to the piezo-electric effect will cause the cantilever to bend, with a bending direction dependent on the alignment of the long axis with respect to the crystal lattice. A cantilever with the long side along [$\bar{1}$10] will, due to the tensile strain along that axis, bend upwards, while a cantilever with the long side aligned with [110] will, due to the compressive strain along that axis, bend downwards.

This is illustrated in 3.7, which shows a finite element method (FEM) simulation of a cantilever being bent due to the piezo-electric effect. An electric potential of 500 V was applied to the nickel electrodes on the top of the GaAs cantilever, while the bottom of the GaAs cantilever was grounded. The z-direction corresponds to the [001] direction, while the x- and y-direction on the two leftmost pictures show respectively the orientation of the [100] and [010]-direction. Two cantilevers were simulated, rotated with 90 degrees with respect to each other along the [001]-plane. It can be seen that, depending on the orientation of the crystal axes, the same electrical potential can cause a cantilever to bend either upwards or downwards.

3.5 Flexoelectricity

The piezoelectric effect consists of a homogenous electric field induced by a homogenous strain or conversely, a homogenous strain induced by a homogenous electric field, and is an effect that only happens in materials without inversion symmetry. However, the presence of a strain gradient breaks up inversion symmetry, and thus any dielectric can have an electric field induced by a strain gradient. The phenomenon of a homogenous electric polarization emerging due to a strain gradient is termed flexoelectricity. The flexoelectric effect was theoretically predicted in the 1950's, but initial interest in the phenomena was limited, since the effect was predicted to be very small. However, experimental studies showed that the flexoelectric coefficients tend to be several orders of magnitude larger than initially predicted, sparking a renewed interest in the field [37]. Furthermore, since strain gradients are dependent on the length scale, the trend of developing ever smaller devices will enable stronger flexoelectric responses.

With strain gradients included, the constitutive equation for the electric polarization in absence of an applied field is [37]

$$P_i = e_{ijk}\epsilon_{jk} + \mu_{klij}\frac{\partial \epsilon_{kl}}{\partial x_j} \tag{3.42}$$

Here, Einstein notation is used, meaning that there is summation over any indice showing up twice in one term. Theoretically, it has been calculated that the number of unique constants in

the flexoelectric tensor μ_{ijkl} can be as high as 54. However, in the case of materials with cubic symmetry the number reduces to three, the transverse flexoelectric coefficient, the longitudinal flexoelectric coefficient and the shear flexoelectric coefficient.

By writing up the 18 partial differential components of the strain gradient in one vector, it ispossible to reduce the flexoelectric tensor to a second rank tensor, which can be represented as a matrix. Then, the polarization induced by the flexoelectric effect can be described as[11]

$$\mathbf{P}_{flexo} = \mu_{3\times 18}\nabla\epsilon_{18\times 1} \tag{3.43}$$

$$\mu_{3\times 18} = \begin{pmatrix}\mu_1 & \mu_2 & \mu_3\end{pmatrix} \tag{3.44}$$

$$\mu_1 = \begin{pmatrix}\mu_{11} & \mu_{15} & \mu_{15} & 0 & 0 & 0\\ 0 & 0 & 0 & 0 & 0 & \mu_{46}\\ 0 & 0 & 0 & 0 & \mu_{46} & 0\end{pmatrix} \tag{3.45}$$

$$\mu_2 = \begin{pmatrix}0 & 0 & 0 & 0 & 0 & \mu_{46}\\ \mu_{15} & \mu_{11} & \mu_{15} & 0 & 0 & 0\\ 0 & 0 & 0 & \mu_{46} & 0 & 0\end{pmatrix} \tag{3.46}$$

$$\mu_3 = \begin{pmatrix}0 & 0 & 0 & 0 & \mu_{46} & 0\\ 0 & 0 & 0 & \mu_{46} & 0 & 0\\ \mu_{15} & \mu_{15} & \mu_{11} & 0 & 0 & 0\end{pmatrix} \tag{3.47}$$

$$\nabla\epsilon_{18\times 1} = \begin{pmatrix}\epsilon_{11,1} & \epsilon_{22,1} & \epsilon_{33,1} & 2\epsilon_{23,1} & 2\epsilon_{31,1} & 2\epsilon_{12,1} & ... & 2\epsilon_{12,3}\end{pmatrix}^T. \tag{3.48}$$

Here the following notation is used

$$\epsilon_{ij,k} = \frac{\partial\epsilon_{ij}}{\partial x_k}. \tag{3.49}$$

If the strain is slowly varying in the x and y directions, meaning that only the gradient of the strain in the Z direction is relevant, the indices of the $\nabla\epsilon_{18\times 1}$ tensor describing the gradient in the X and Y direction will be zero, allowing the following simplification to be carried out

$$\begin{pmatrix}P_x\\ P_y\\ P_z\end{pmatrix} = \begin{pmatrix}0 & 0 & 0 & 0 & \mu_{46} & 0\\ 0 & 0 & 0 & \mu_{46} & 0 & 0\\ \mu_{15} & \mu_{15} & \mu_{11} & 0 & 0 & 0\end{pmatrix}\begin{pmatrix}\epsilon_{xx,z}\\ \epsilon_{yy,z}\\ \epsilon_{zz,z}\\ 2\epsilon_{yz,z}\\ 2\epsilon_{zx,z}\\ 2\epsilon_{xy,z}\end{pmatrix}. \tag{3.50}$$

With $\epsilon_{yz} \approx \epsilon_{zx} \approx 0$, the flexoelectric effect reduces to

$$P_z = \mu_{15}\epsilon_{xx,z} + \mu_{15}\epsilon_{yy,z} + \mu_{11}\epsilon_{zz,z}. \tag{3.51}$$

The values of the flexoelectric tensors for Gallium Arsenide have not been measured experimentally, and it is known for other materials that the theoretical estimates and experimental measured values of the flexoelectric coefficients tend to have a discrepancy of roughly three orders of magnitude, with the measured value being the larger one[13].

The best current theoretical estimates for the flexoelectric tensor values for Gallium Arsenide are [11]

$$\mu_{15} = -0.84\,\text{nC/m}, \quad \mu_{11} = 0.51\,\text{nC/m}, \quad \mu_{46} = 0.27\,\text{nC/m}. \tag{3.52}$$

3.6 Franz-Keldysh Effect

Direct bandgap semiconductors are capable of absorbing light with wavelength energies above the bandgap. For a waveguide made of a direct bandgap semiconductor with bandgap energy E_g, the light-matter interaction can have two conditions. Photons with energies above the bandgap energy, $E > E_g$, are capable of exciting an electron from the valence band to the conduction band, creating an electron-hole pair. This facilitates electrical conduction in the semiconductor, while also making the semiconductor opaque for that wavelength. In the absence of an applied electric field, photons with energies below the bandgap, $E < E_g$ fail to excite an electron-hole-pair, and the semiconductor can be considered transparent for that wavelength, and one or more guided modes will exist.

The solution of the Schrödinger equation for a particle in a periodic potential is the Bloch function, which consist of the wave equation for a particle in free space modulated by a function with the same periodicity as the Hamiltonian. This is a fundamental result in condensed matter physics and is the basis for the energy band model. If a strong electric field is applied to the semiconductor, the potential given by the Hamiltonian does no longer have the periodicity of lattice spacing, and so the Bloch functions are no longer solutions [27]. This results in the absorption edge being "smeared" out, allowing for absorption of photons with energies $\hbar\omega$ below the bandgap energy E_g.

In this effect, which is termed the Franz-Keldysh effect, the absorption for energies below the bandgap at a given applied field strength F is given by

$$\alpha(E,F) = \alpha_b \beta^{1/2} \pi \left[\left(\frac{\partial \mathrm{Ai}(-\xi)}{\partial(\xi)} \right)^2 + \xi \mathrm{Ai}^2(-\xi) \right], \tag{3.53}$$

where ξ is the dimensionless variable

$$\xi = \frac{\hbar\omega - E_g}{\beta}, \text{ with } \beta = \left(\frac{\hbar^2 e^2 F^2}{2m_r} \right)^{1/3}. \tag{3.54}$$

Here β is the characteristic energy, F is the applied field and m_r is the reduced effective mass of the electron-hole combination

$$m_r = \frac{m_h m_e}{m_h + m_e}, \quad m_{r,GaAs} = 0.059\, m_0, \tag{3.55}$$

and α_b is

$$\alpha_b = \frac{q^2 x_{vc}^2}{\lambda_0 \epsilon_0 \hbar^3 n_{op}} (2m_r)^{3/2}. \tag{3.56}$$

This is also used in the absence of an applied electric field, where the frequency-dependent absorption coefficient is

$$\alpha(F = 0, \omega) = \alpha_b \sqrt{\hbar\omega - E_g}. \tag{3.57}$$

Central to the behaviour of the Franz-Keldysh effect is the Airy function, which is the solution to the differential equation

$$\frac{\partial^2 \mathrm{Ai}(x)}{\partial x^2} - x \cdot \mathrm{Ai}(x) = 0. \tag{3.58}$$

Here the Airy function is

$$\mathrm{Ai}(x) = \frac{1}{\pi} \int_0^\infty cos(t^3/3 + xt) dt \tag{3.59}$$

This solution satisfies the condition $\mathrm{Ai}(x) \to 0$ as $x \to \infty$

This Airy function, which is the solution to important differential equations describing phenomena in quantum mechanics and optics, should not be confused with the similarly named circular Airy function or Airy discs, which describe the optical diffraction pattern caused by an optical point source.

The behavior of this Airy function is strongly regime dependent, and can be seen on figure 3.8. For $x < 0$, the Airy function oscillates with a decreasing period and magnitude,

$$\mathrm{Ai}(x) \approx \frac{1}{2\sqrt{\pi}x^{1/4}} \sin\left(-2/3x^{2/3} + \frac{\pi}{4}\right), x \to -\infty \tag{3.60}$$

In semiconductors with a powerful applied electric field, this is the cause of above-band oscillations for $\xi = \hbar\omega - E_g > 0$.

For $x > 0$, the Airy function rapidly decays in an exponential manner

$$\mathrm{Ai}(x) \approx \frac{1}{2\sqrt{\pi}x^{1/4}} \exp\left(-2/3x^{2/3}\right), x \to \infty \tag{3.61}$$

For energies below the bandgap, $\mathrm{Ai}(-\xi)$ will be in the exponentially decaying regime, meaning that the conduction band will be smeared out. The Franz-Keldysh effect is is a relatively weak effect, requiring electric fields with an order of magnitude of $1 - 100$ kV/cm in order to have significant effect on absorption.[35]

In figure 3.9, the Franz-Keldysh absorption can be seen for respectively several different wavelengths depending on the field, and for several different fields depending on the wavelength.

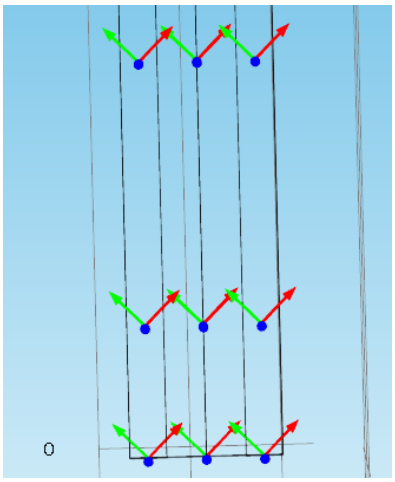

(a) Long side along [110], short side along [1$\bar{1}$0]

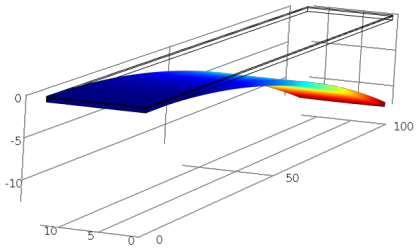

(b) Long side along [110], short side along [1$\bar{1}$0]

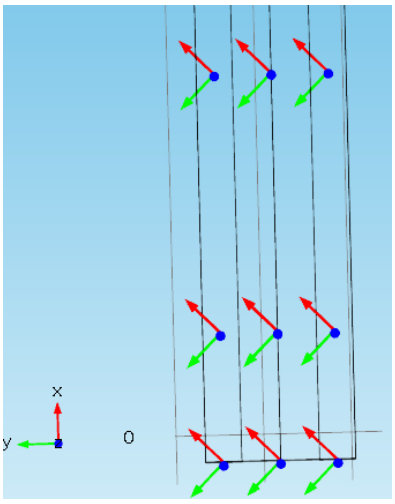

(c) Long side along [1$\bar{1}$0], short side along [110]

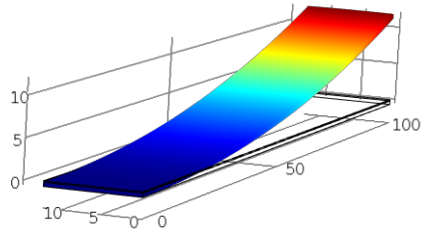

(d) Long side along [1$\bar{1}$0], short side along [110]

Figure 3.7: The result of application of a positive voltage for cantilevers cut along different directions.

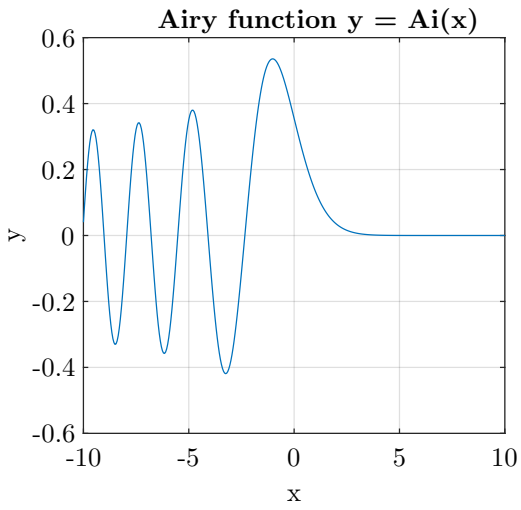

Figure 3.8: The Airy function.

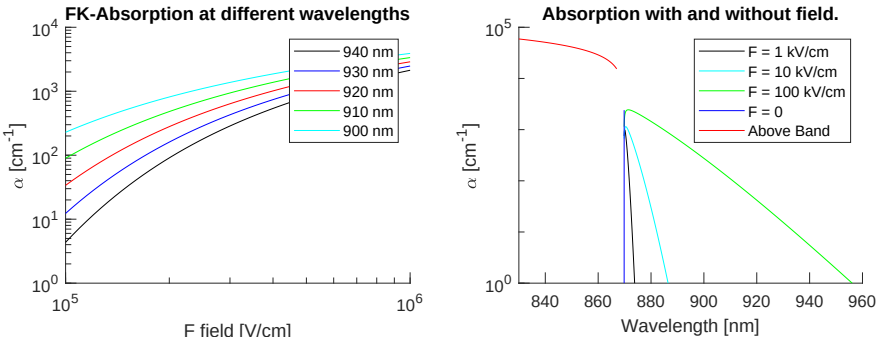

Figure 3.9: Frank-Keldysh absorption for different fields and wavelengths.

Chapter 4

Finite element method simulations

In order to achieve an understanding of the mechanics of the device, numerical simulations using the finite element software COMSOL were carried out. In one simulation a realistic model of the curved bilayer cantilever is built, and a strain is induced by applying an electric potential to the Nickel layer of the cantilever. From here, the piezo-electrically induced band gap shift in the Gallium Arsenide waveguide induced in chapter 3 is calculated using the Pikus-Bir Hamiltonian, allowing for a discussion of the potential for strain tuning of the position and bandgap of the device. In the other simulation built during this thesis, a flat bilayer cantilever is built, corresponding to the device before release. Intrinsic stress is then applied to ether the Nickel or the GaAs layer of the device, and then resulting strain in the GaAs waveguide is analyzed. From this, the intrinsic band gap shift of the device and the is discussed.

4.1 Simulation of strains in curved waveguide.

Mismatch between the intrinsic stresses in the GaAs and metal layers will lead to bending [23]. Given that the curved cantilever waveguide consists of a formerly flat GaAs-Ni bilayer cantilever which is rolled up, there is large and inhomogenous strains to be found inside the waveguide. A schematic of model used can be seen on figure4.1, and an illustration of the model used can be seen on figure 4.2. In this section, simulations are carried out on a flat bilayer model of the cantilever waveguide with intrinsic stress applied to the x-y direction, mimicking either an uniform expansion or compression. Since intrinsic stress on the GaAs layer would lead to a change in the minimum allowed energy for the waveguide, the model used has entirely intrinsic tensile stress on the Ni layer. By sweeping over a range of values for the intrinsic stress, the intrinsic stress necessary to obtain a radius of curvature of 78 μm, which identical to that of the characterized devices, is obtained. The strains in the cantilever waveguide are extracted, and from them the bandgap shift as well as the electric field caused by the piezo-and flexo-electric effect from the strain and the strain gradient is investigated.

4.1.1 Deriving the needed stress

For a GaAs-Ni bilayer cantilever where the GaAs and Ni layer have the same thickness, the relationship between the radius of curvature and strain mismatch is, as mentioned in chapter 3,

$$\frac{1}{\rho} = \frac{24\epsilon}{d[12 + (1+n)(1+n^{-1})]} \leftrightarrow \epsilon = \frac{d[12 + (1+n)(1+n^{-1})]}{\rho}. \tag{4.1}$$

For a radius of curvature 78.1 μm, thickness $d_1 = d_2 = 160$nm for both layers, resulting in $d = d_1 + d_2 = 320$nm and $m = d_1/d_2 = 1$, and a Young's Modulo ratio

$$n = \frac{E_1}{E_2} = \frac{E_{Ni}}{E_{GaAs}} = \frac{219 \cdot 10^9 \text{GPa}}{84.8 \cdot 10^9 \text{GPa}} = 2.582. \tag{4.2}$$

The strain mismatch becomes

$$\epsilon = \frac{320 \cdot 10^{-9}\text{m}[12 + (1 + 2.582)(1 + 2.582^{-1})]}{24 \cdot 78.1 \cdot 10^{-6}\text{m}} = 2.90 \cdot 10^{-3}. \tag{4.3}$$

For Ni, the non-zero indices of the stiffness matrix are as following[28]

$$C_{11,Ni} = 2.481 \cdot 10^{11}\text{ Pa}, C_{12,Ni} = 1.549 \cdot 10^{11}\text{ Pa}, C_{12,Ni} = 1.242 \cdot .10^{11}\text{ Pa} \tag{4.4}$$

The strain mismatch is $\epsilon = (l_{GaAs} - l_{Ni})/l_{Wg} = \epsilon_{Ni} - \epsilon_{GaAs}$. If it assumed that the stress entirely on the Ni layer, the intrinsic stress on each of these layers can be found using the stiffness matrix.

$$\sigma_{11,Ni} = C_{11,Ni}\epsilon_{11} + C_{12,Ni}(\epsilon_{22} + \epsilon_{33}) = (C_{11,Ni} + C_{12,Ni})\,\epsilon \tag{4.5}$$

$$= \left(2.481 \cdot 10^{11}\text{ Pa} + 1.59 \cdot 10^{11}\text{ Pa}\right) \cdot (2.90 \cdot 10^{-3}) = 1.14\,\text{GPa}. \tag{4.6}$$

For a simple bilayer cantilever, the intrinsic biaxial stress that will result in a bending radius of 78 μm is thus $\sigma_{Ni} = 1.14\,\text{GPa}$. This case is a simpler model than the one used in the simulation, which is a cantilever waveguide tethered to two bilayer cantilevers, and thus this prediction is not necessarily describing the reality. Compared to the analytical predictions, the models required a far higher stress on the Nickel layer in order to reach a circular curvature. A likely explanation is that the theoretical prediction is for a simple bilayer cantilever, while the cantilever used likely due to the fact that the GaAs layer is larger than the Ni layers.

The needed stress on Ni was found by running a auxillary sweep in COMSOL over a variety of strains.

For σ_{GaAs}, the intrinsic biaxial stress that was found to cause a circular bending was $-4 \cdot 10^8\,\text{Pa}$, while the intrinsic biaxial stress that caused a circular bending for σ_{Ni} was $5 \cdot 10^9$ Pa.

4.1.2 Bandgap shift in waveguide with intrinsic stress

In figure 4.3, the strain components, measured at the middle, bottom and top of the GaAs cantilever can be seen. On this figure, the waveguide tethers are shown with grey lines. $\epsilon_{xx} = \epsilon_{yy} \approx -\epsilon_{zz}$ for waveguide. It can be seen that the strain varies wildly between two tether bridges, and the strain components cross each other. On the model, it can also be seen that, due to the Ni attempting to compress, the GaAs cantilever bulges out between the tether bridges. Since the shear strain component ϵ_{xy} is large, the here will be a coupling between the two split-up valence band states. The two separate eigenstates to the 4×4 Pikus-Bir Hamiltonian are thus no longer purely heavy or purely light holes.

On figure 4.4, the energy shifts induced by the strain can be seen. Of these shifts, especially the negative bandgap shift at the bottom of the cantilever waveguide is of interest. The guided mode, while located mostly ind the middle, is smeared out over the entire waveguide. This, combined with the fact that the coefficient for above bandgap absorption is extremely high and of an order of magnitude $\alpha\tilde{1}0^4\ \text{cm}^{-1}$[25].

For the used spectrometer, the maximum measurable intensity before saturation was $I_{max} = 7{\cdot}10^4\text{s}^{-1}$. Meanwhile, a constant background noise was measured at$I_{noise} = 350\text{s}^{-1}$. If attenuation filters are placed before the fiber coupler leading to the spectrometer in order to prevent overflow,

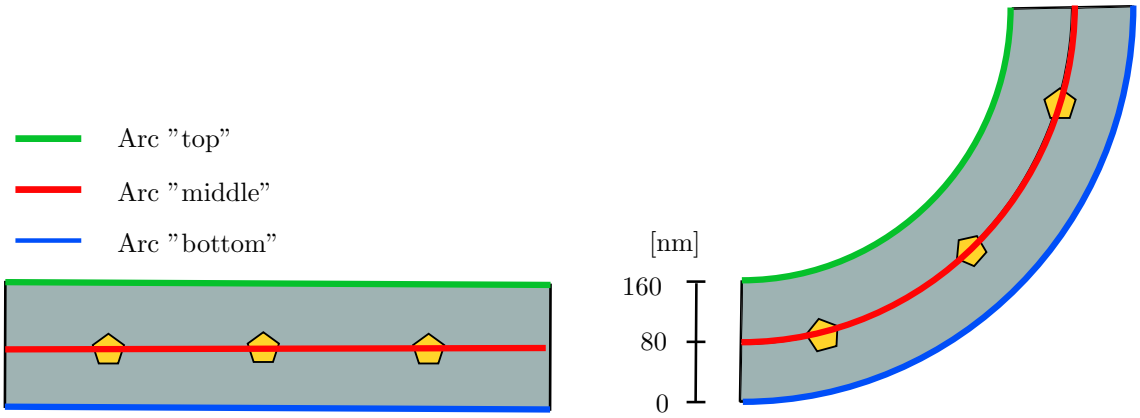

Figure 4.1: Schematic of the flat cantilever model

Figure 4.2: Designed model of the flat cantilever waveguide. This waveguide has, similar to waveguides characterized in the laboratory, a tether distance of 10 μm and a tether width of 0.2 μm. On the large figure, the units on the axes are all in μm.

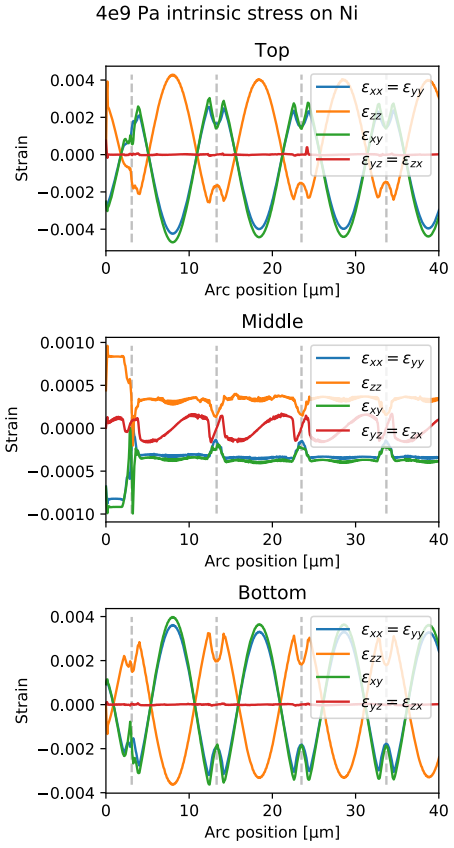

Figure 4.3: Strain in the waveguide for stressed Ni. The dashed grey lines shows the position of the tethers connecting the waveguide to the bilayer cantilevers.

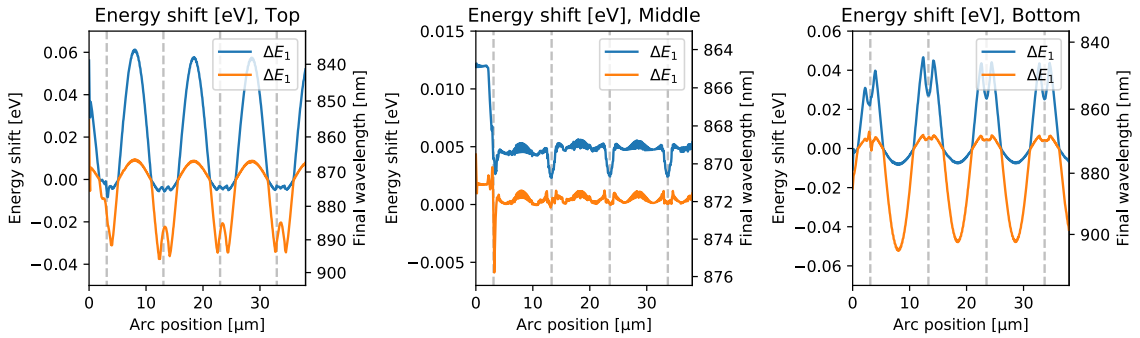

Figure 4.4: The result for stressed Ni. The final wavelengths assume initial absorption edge of 872 nm

total absorption can be estimated to be $\frac{I_{noise}}{I_{max}} = 200^{-1}$. With this definition of total absorption, and a low estimate for the absorption coefficient $\alpha = 8000\,\mathrm{cm}^{-1}$, then the length x needed for total absorption can be found by using

$$\frac{I_{out}}{I_{in}} = \mathrm{e}^{-x\cdot\alpha} \rightarrow x = \frac{-\ln\left(\frac{I_{out}}{I_{in}}\right)}{\alpha} \tag{4.7}$$

$$x = \frac{-\ln\left(200^{-1}\right)}{8000\,\mathrm{cm}^{-1}} = 6.63\cdot 10^{-4}\,\mathrm{cm} \tag{4.8}$$

With these assumptions, the light thus only needs to pass through 6.63 μm of the part of the waveguide with high absorption in order to be completely extinguished. A set of cantilever waveguides with radius of curvature $\rho = 78\,\mu$m, the total length of the bent parts of the waveguide is $2\cdot 78\,\mu\mathrm{m} = 244.9\,\mu$m. With a tether distance $10\,\mu$m, this gives 24 tethers per structure. Thus, on average a guided mode needs only $0.27\,\mu$m of area with above-bandgap absorption in order to fulfill this criteria for complete extinction. From these simulations, it can be concluded that intrinsic tensile stress exclusively on the Ni layer will cause a strain on the GaAs cantilever waveguide that is very highly dependent on the position in the waveguide, both vertically and along the waveguide, while the intrinsic stress on the GaAs will cause a strain that is mostly independent of both vertical and longitudinal position.

4.1.3 Franz-Keldysh

In order to find the smear caused by the Franz-Keldysh effect, the strain and strain gradient in the simulation of a waveguide with intrinsic stress was measured.

In figure 4.5, slice plots of the strain component can be seen. In this simulation, N initial tensile stress have been applied to the nickel strips. It can bee seen that the strain gradient in all directions but Z is negligible, simplifying the calculations needed for extracting the flexoelectricity, and additionally the complexity of the code.

The magnitude of the stress that caused a circular bend in the simulation was identified. For this stress, z-y plane slice plots of the six strain parameters spanning the crosssection of the waveguide were exported into COMSOL. These slice plots spanned the entire length of the cantilever with regular intervals. Code was written to extract the data from the slice plot in the middle between the two tether bridges, since that was where the strain was found to be strongest.

In figure 4.7, an estimate for the size of the piezo-electric field as well as the smaller correction from the flexoelectric effect can be seen. The plots are measured down the middle of a cross-section of the waveguide. It can be seen how total electric fields are surprisingly large, at an order

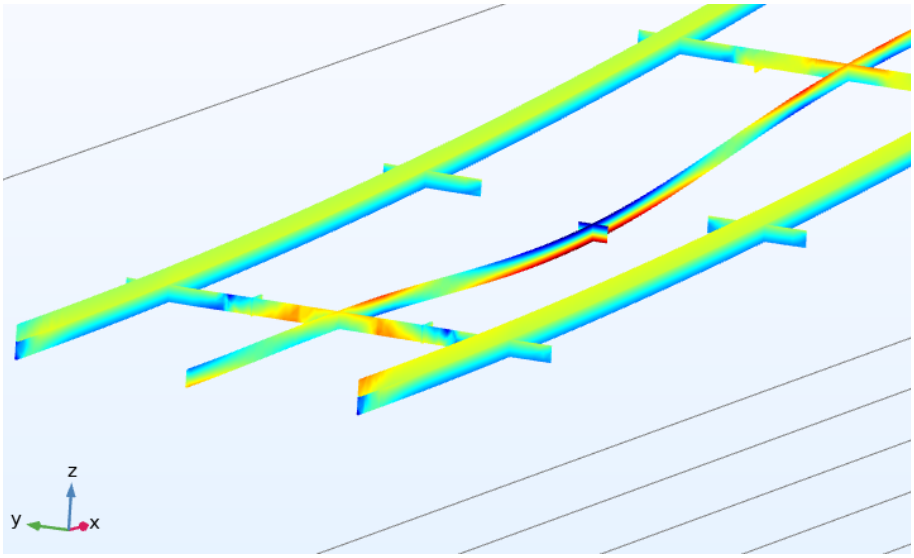

Figure 4.5: Illustration of a finished simulation where the strain was on the Ni

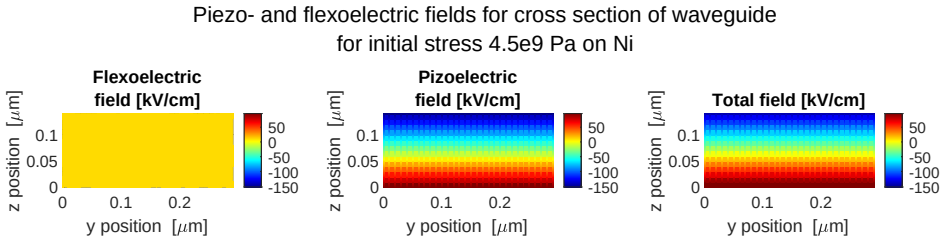

Figure 4.6: Flexo-electric and piezoelectric fields.

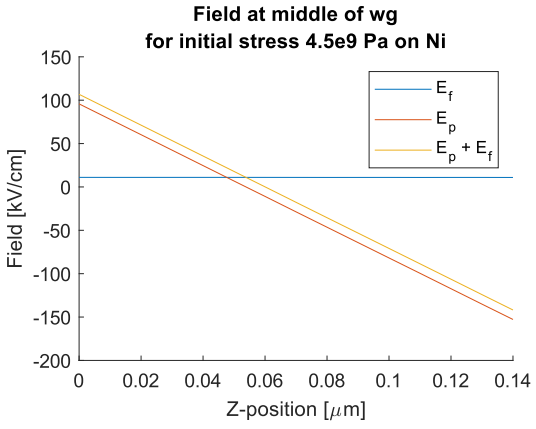

Figure 4.7: Field down middle

of $\tilde{1}00$ kV/cm depending on the vertical position in the waveguide. The flexoelectric contribution is also rather large, at 11 **kV/cm**. This has to be contrasted with the fact that while this is using theoretical estimations of the GaAs flexoelectric coefficients, it is known that experimental values tends to be several orders of magnitude larger[37]. The flexoelectric induced field is linearly dependent on the flexoeletric parameters, and it is thus possible that the electric field in the cantilever should be much larger than this estimate.

The size of the field in the cantilever waveguide is thus, especially away from the center, of the order of magnitude where the Franz-Keldysh effect starts to greatly influence the optical absorption[35],and thus a sloping extinction will likely be seen rather than a sharp absorption edge.

4.1.4 Summary on simulation on flat stressed waveguide

A large intrinsic stress of $4 \cdot 10^9$ Pa was necessary in order to obtain a circular curvature for the bending. This large stress lead to large strain components causing a large

4.2 Simulation on piezo-electrical tuning of bent cantilever waveguide

Two different models are constructed. On the first one, an electric potential is applied to the nickel electrodes of a circular curved cantilever waveguide to illuminate the possibilities of piezo-electrically tuning the position of the coupler as well as the GaAs bandgap. In the second one, intrinsic stress is applied to either the GaAs layer or the Ni layer of a flat bilayer cantilever. With this model, the stress needed in order to reach a vertical position is examined, and compared to the theoretical calculations. Furthermore, the strains in the GaAs waveguide caused by this intrinsic stress are extracted from the model, and the effect it can have on GaAs optical properties are examined. This is done by calculating the strain-induced bandgap shift using the Pikus-Bir Hamiltonian as well as by calculating the flexoelectric and piezoelectric fields induced by the strain, and then finding the sub-bandgap absorption this will induce according to the Franz-Kerdysh theory of electroabsorption. In the characterization section, the results obtained in the experiments are compared to the results in this simulation, and the validity of the stress-on-GaAs model vs the stress-on-Ni-model is discussed.

In the computational section of this thesis, I strived after building a COMSOL model as close to reality as possible. The main challenge of building the simulation itself showed up in two different places - constructing the holes in the pre-curved waveguide, and constructing a coordinate system describing the orientation of the material crystal axes in the pre-curved waveguide.

4.2.1 Constructing the geometry

In the model with the pre-curved waveguide, a single GaAs cantilever waveguide with tethers on each side connecting it to GaAs-Ni bilayer cantilevers is defined. The waveguide has a circular curvature.

Initial attempts at building the waveguide featured three separate GaAs cantilevers, which were then connected with tethers, however this approach was unsuccessful. Instead, a model was developed where a single, curving sheet of GaAs was defined, and layers of Ni were placed on top at the edges. Then, a COMSOL part consisting of a "tether hole" was defined. This hole is robustly defined, allowing for quick change of spatial parameters in the simulation. First, the part is built, lying in the origo. after which it is rotated and translated, placing it on both sides of the cantilever like pearls on a string. The stencil overlaps with the GaAs layer and can, using the Difference boolean expression, be used to delete the intersection as well as the part of the stencil

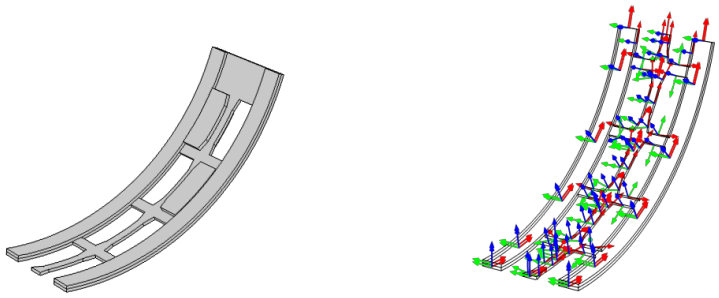

(a) Illustration of a not-to-scale cantilever with the stencils partially punched out.

(b) A not-to-scale version of the waveguide with curvilinear coordinates. Note how the system bends around the tethers

Figure 4.8: Illustrations of not-to-scale models of the curved waveguide.

sitting outside the waveguide. A waveguide with partially punched-out holes can be seen in figure 4.8a.

4.2.2 Coordinate system

Since the piezo-electric effect is dependent on the orientations of the stress and strain directions, or conversely what direction the electric field is applied to, with respect to the crystal orientations, building a coordinate system in COMSOL that describes the position-dependent orientation of the crystal axes is a must. Defining the curved cantilever shape and marking Gallium Arsenide as its material will cause the cantilever to be regarded as if carved out of a solid block of GaAs rather than consisting of a flat sheet of GaAs which has acquired a bending.

While COMSOL has built in support for creating a curvilinear coordinate system, this is not what should be used in this case. The curvilinear coordinate systems in COMSOL are built to define flow, such as heat diffusion, fluid flow or electrical current flow, through a system. The different methods of defining a curvilinear coordinate system in COMSOL are all based on defining a vector field through the system by defining an inlet and an outlet[7]. While the curvilinear coordinate system can in some cases be used for anisotropic materials, such as for creating a deformed cylindrical coordinate system for describing bending fibers such as arteries, coaxial waveguides and multiturn coils, this assumes that the anisotropy of the material has cylindrical symmetry. An illustration of a coordinate system for the bent cantilever built using COMSOLs Curvilinear coordinate system function can be seen in figure 4.8b.

In the model of the waveguide, the "holes" in the cantilever would prevent this from working, since the coordinate system formula would consider them part of the flow, and the coordinate system would be distorted. Furthermore in the COMSOL Curvilinear coordinate system, one of the components (the x-component) of the curvilinear coordinate system is always parallel with the streamlines, and the two other normal to the streamlines. In my simulation, the GaAs cantilever is made of a cantilever cut along the [110] edge, and the directions of the coordinate system are thus at a $\pm\pi/4$ angle rather than respectively parallel and normal.

Instead, in order to define the cantilever waveguide, an analytical expression for the orientation of the GaAs depending on the position must be derived. This is used by first defining two separate coordinate systems, one using the COMSOL Base Vector Coordinate System function, which defines the bending of the waveguide at a given x-position, and one describing the $\pi/4$ rotation in the x-y plane. The two transformation tensors can then be multiplied to form one transformation

tensor.

When using more than one coordinate system transformation on a tensor $\mathbf{v}$ the order of the applied transforms must be

$$\mathbf{Q}^T\mathbf{R}^T\mathbf{vRQ} = (\mathbf{RQ})^T\mathbf{vRQ} = \mathbf{S}^T\mathbf{vS}. \tag{4.9}$$

The transformation matrix describing a coordinate system being rotated θ is

$$rot(\theta) = \begin{pmatrix} \cos(\theta) & \sin(\theta) & 0 \\ -\sin(\theta) & \cos(\theta) & 0 \\ 0 & 0 & 1 \end{pmatrix}, \qquad rot(\theta = -\pi/4) = \begin{pmatrix} \frac{1}{\sqrt{2}} & -\frac{1}{\sqrt{2}} & 0 \\ \frac{1}{\sqrt{2}} & \frac{1}{\sqrt{2}} & 0 \\ 0 & 0 & 1 \end{pmatrix} \tag{4.10}$$

After a circular bending with radius of curvature ρ from flat, the element of the waveguide at position x will have a direction of

$$V(x) = \begin{pmatrix} \rho \cdot \sin(\phi) \\ 0 \\ \rho(1 - \cos(\phi)) \end{pmatrix}. \tag{4.11}$$

Here $\sin(\phi) = \frac{-x}{r}$, and $\cos(\phi) = \sqrt{1 - \left(\frac{x}{r}\right)^2}$

The coordinate system transformation tensor will become

$$\begin{pmatrix} \cos(\phi) & 0 & -\sin(\phi) \\ 0 & 1 & 0 \\ \sin(\phi) & 0 & \cos(\phi) \end{pmatrix} = \begin{pmatrix} \sqrt{1 - \left(\frac{x}{\rho}\right)^2} & 0 & \frac{x}{\rho} \\ 0 & 1 & 0 \\ -\frac{x}{\rho} & 0 & \sqrt{1 - \left(\frac{x}{\rho}\right)^2} \end{pmatrix}. \tag{4.12}$$

Multiplying the two coordinate transformation tensors together, the result is

$$\mathbf{T}_{[110]} = \begin{pmatrix} \frac{1}{\sqrt{2}}\sqrt{1 - \left(\frac{x}{r}\right)^2} & \frac{-1}{\sqrt{2}} & \frac{1}{\sqrt{2}}\left(\frac{x}{r}\right) \\ \frac{1}{\sqrt{2}}\sqrt{1 - \left(\frac{x}{r}\right)^2} & \frac{1}{\sqrt{2}} & \frac{1}{\sqrt{2}}\left(\frac{x}{r}\right) \\ -\frac{x}{r} & 0 & \sqrt{1 - \left(\frac{x}{r}\right)^2} \end{pmatrix}. \tag{4.13}$$

This describes the orientation of the crystal axes [100], [010] and [001] depending on the position. Conversely, if the cantilever is defined with the long axis along $[\bar{1}10]$, the coordinate system becomes

$$\mathbf{T}_{[\bar{1}10]} = \begin{pmatrix} \frac{1}{\sqrt{2}}\sqrt{1 - \left(\frac{x}{r}\right)^2} & \frac{1}{\sqrt{2}} & \frac{1}{\sqrt{2}}\left(\frac{x}{r}\right) \\ \frac{-1}{\sqrt{2}}\sqrt{1 - \left(\frac{x}{r}\right)^2} & \frac{1}{\sqrt{2}} & \frac{-1}{\sqrt{2}}\left(\frac{x}{r}\right) \\ -\frac{x}{r} & 0 & \sqrt{1 - \left(\frac{x}{r}\right)^2} \end{pmatrix}. \tag{4.14}$$

In figure 4.9, the built coordinate system can be seen. Due to being specified as the material coordinate system of the material, it will move with the material, and will thus not be recalculated with the new coordinates after deformation. This coordinate system, however, does not work for positions $x \geq r$, since that will lead to taking the square root of a negative number. When carrying out the simulation, this also requires the bending of the waveguide to be less than $\pi/2$ since otherwise, the FEM simulation will fail while the bending is simulated.

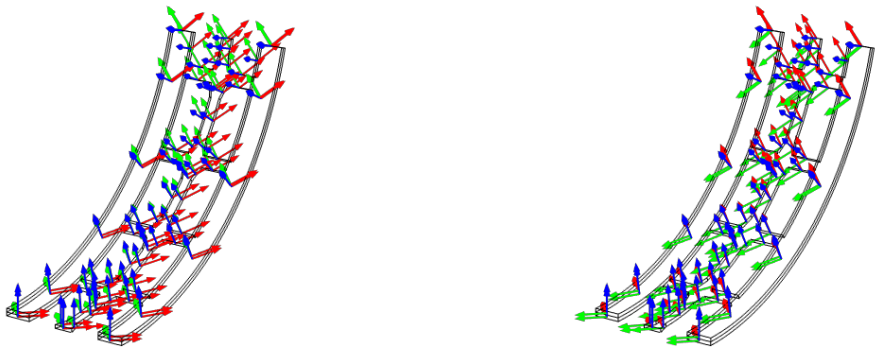

(a) Crystalline coordinate system for Cantilever with long edge along [110]

(b) Crystalline coordinate system for Cantilever with long edge along [$\bar{1}$10]

Figure 4.9: The two coordinate systems, for cantilevers with the long side along respectively [110] and [$\bar{1}$10]. The red, green and blue arrows are the x, y and z direction in the material coordinate system which correspond to respectively the [100], [010] and [001] crystal axis

4.2.3 Piezo-electrical tuning of bandgap in circularly bent cantilever

In this section, the piezoelectrical tuning of bulk GaAs band gap in a circularly curved cantilever waveguide is simulated.

The waveguide here defined as circular and curved, and is assumed to not have any intrinsic strain. An electric potential of $V_{pot} = 3\,\mathbf{V}$ is added to the Nickel layer on top of the waveguides, with this value being chosen since this is the largest the wafer can handle without breaking down. A simulation of the piezo-electric effect is then run, and the strain is extracted along pre-defined parametric lines placed at several different vertical positions inside the waveguide, and with a curvature matching that of the waveguide. An illustration of the final model used for the simulations can be seen in figure 4.10, with close-ups showing the bilayer waveguide, and the positions of the parametric lines. Early simulations showed that the strain did not vary horizontally, and thus the investigation focused on the strain in different vertical positions.

The strain components are then exported, and the bandgap shift caused by that strain is calculated in Python by solving the 4x4 reduced Pikus-Bir Hamiltonian (Eq. 3.28) analytically. The influence of tether distance, cantilever width and orientation of the device is examined.

4.2.4 Different Orientations of the waveguide

First, it was investigated whether or not the orientation of the waveguide along the crystal axis would have an influence on the bandgap shift. Two simulations were run, one where the waveguide had the long side along [110], and one where the waveguide had the long side along [1$\bar{1}$0]. For both of these simulations, an electric potential of 3 V was applied to the interface between the Nickel layer and the GaAs layer, simulating a potential being applied to a metal electrode connected to the Nickel strips. The simulation was then run using the COMSOL piezo-electric module.

The waveguide that had the long side along [110] curled upwards as a result of the Piezo-electric effect, while the waveguide that had the long side along [1$\bar{1}$0] curled downwards, ad shown in figure. The total displacement of the waveguide was 0.4 μm, which doubles to 0.8 μm when accounting for the fact that the possible applicable voltage is in the range $\pm$3 V. Since the waveguide has a height of 160 nm, this means that the waveguide tip is moved 35 times longer than it is tall, showing

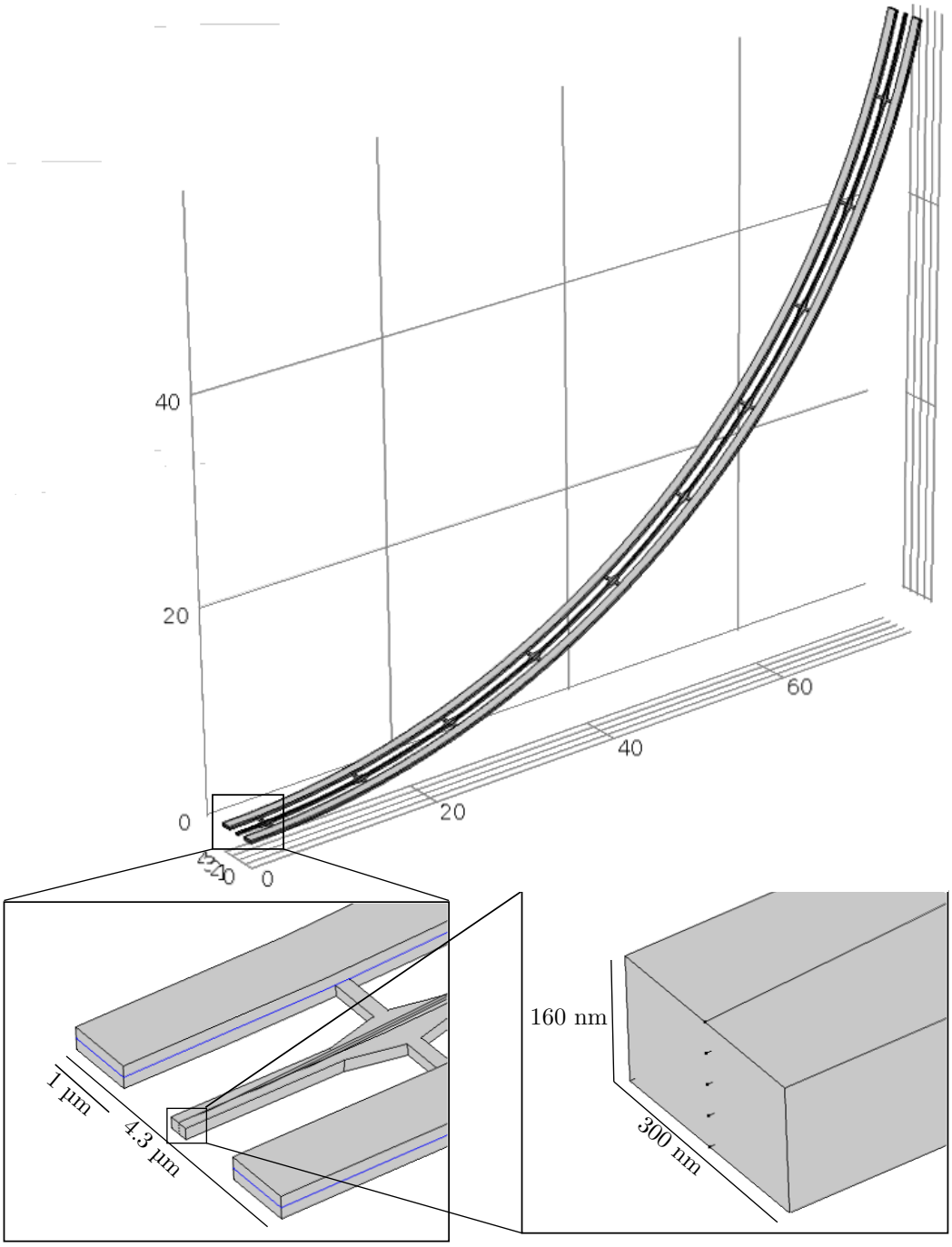

Figure 4.10: Designed model of the cantilever waveguide. This waveguide has, similar to waveguides characterized in the laboratory, a tether distance of 10 μm and a tether width of 0.2 μm. On the large figure, the units on the axes are all in μm.

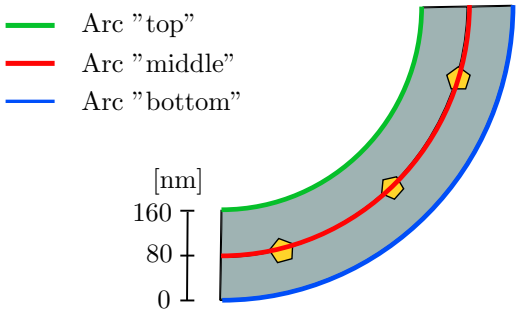

(a) Illustration of the bent cantilever

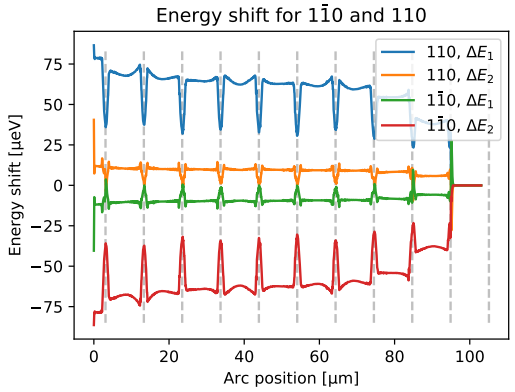

(b) Energy shift for cantilever along [110], [1$\bar{1}$0]

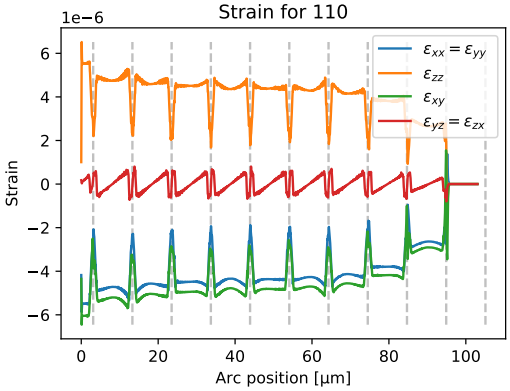

(c) Strains for cantilever along [110]

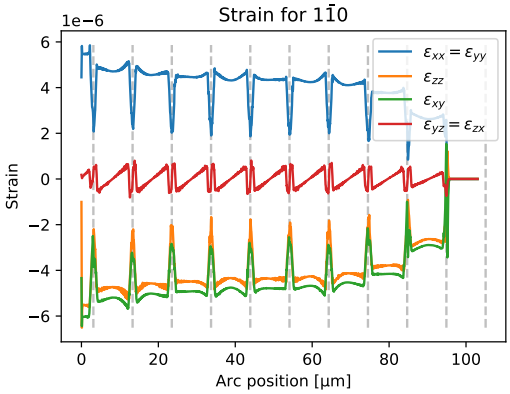

(d) Strains for cantilever along [1$\bar{1}$0]

Figure 4.11: Simulation results for cantilevers with different crystal orientations.

the potential of using this technology to move a cantilever waveguide in and out of a beam spot. This potential, however, is strongly restricted by the size of said beam spot, which can easily be micrometers in size when focused. However, this still shows potential for finetuning the optimal alignment of the cantilever tip in the beam spot.

The major difference between the strains for [110] and [1$\bar{1}$0], is that for the [110] case $\epsilon_{xx} = \epsilon_{yy}$ are negative, while for the [1$\bar{1}$0] they are positive. For the [110], both states acquire a positive shift in energy, with the state 1 getting a large positive shift and the state 2 getting a small positive shift. For the [1$\bar{1}$0], both states acquire a negative shift in energy, with the state 1 getting a small negative shift and the state 2 getting a large negative shift.

4.2.5 Summary of simulation on curved waveguide

Applying an electric potential to the nickel on the curved bilayer cantilever waveguide induces an electric field in the GaAs layer, which induces a bending via the piezoelectric effect. This bending both moves the tip of the waveguide, meaning that it can be used for adjusting the position of the coupler, and changes the emission level, however slightly, of the embedded quantum dots.

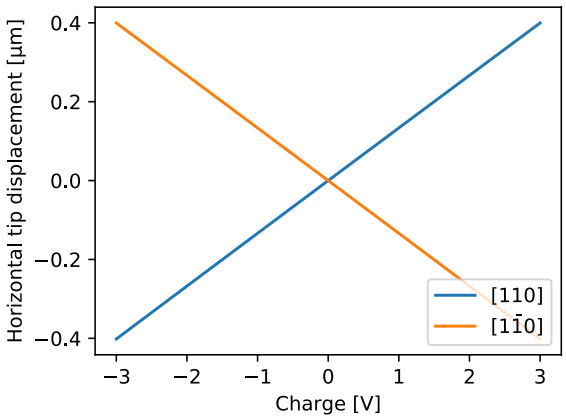

Figure 4.12: Displacements of the tether tips dependent on the electric potential applied to the nickel and the crystal axis the long side is aligned with.

Chapter 5

Fabrication

Integrated photonic circuits are too small to be designed by hand, and instead complex machinery is used to define the design, etch patterns and lay down strips of material. Over the years, more and more sophisticated instruments have been developed, decreasing the minimum length scales while increasing precision and yield.

In this chapter, the basics of photonic microfabriction are laid out. The wafer used for the experimental parts of this thesis is a GaAs wafer, which is advantageous for integrated photonics due to its direct bandgap, allowing effective incorporation of quantum dot single photon sources. At the top, there is a 160 nm thick GaAs layer with embedded quantum dots. Underneath, there is an 1150 nm thick layer of AlGaAs, which acts as a sacrificial layer, which again lies on top of an underlying GaAs substrate.

The devices used for this thesis are fabricated in a three step process. In the two steps, a positive CSAR resist is used. For the first step, thin strips are defined in the mask, allowing the deposition of the metal strips causing the bending effect of the waveguides. In the second step, the waveguides and cantilevers are carved out using dry etching. In the third step, a negative epoxy resist is used. During exposure, the cladding on the tips are defined. The rest of the epoxy, save the markers used for the nonius, is removed during development, and the epoxy is hardened with a hard bake. Finally, a wet etching using HF is carried out. This carves out the undercut, suspending the waveguides and freeing the cantilevers, which curl up to release the intrinsic stress.

Typical final thicknesses for the resists are $\tilde{5}$00nm for metal deposition, $\tilde{4}$00nm for deep etchings and $\tilde{1}$100 nm for the negative resist used for epoxy cladding.

The recipe used for the samples used in this thesis consists of four steps:

- First electron beam exposure followed by metal deposition and lift-off
- Second electron beam exposure followed by dry etching, defining the waveguides
- Third electron beam exposure with negative epoxy resist, placing epoxy tips on waveguide.
- Cleaning, wet etching to remove AlGaAs layer under suspended waveguides, followed by critical point drying.

5.1 Lithography

A fundamental method in micro- and nanofabrication is lithography. The sample is covered in a thin film consisting of a polymer resist, which is placed on the chip using a technique called spin-coating. During spin-coating, the chip is placed on a mount containing hole in the center, after which a vacuum is created, keeping the chip in place. A few drops of the resist is then placed

on the chip, after which the spin coater begins to rapidly rotate with a rotation speed in the order of $\tilde{1}0^3$ rpm. This disperses the resist on the sample surface, creating an even layer with a thickness which is thicker the more viscous the resist is, and thinner the larger the rotation speed is and the longer the time spent spinning is.

Under a process called exposure, a pattern is then transferred onto the rest either by the means of UV light filtered through a physical photomask or by a focused electron beam drawing a pattern defined by a computer program. For a positive resist, the exposed areas are made more soluble, while a negative resist becomes less soluble when exposed. After this, the sample is immersed in a liquid known as a developer, which removes the non-exposed areas of the chip for a negative photoresist, or the exposed areas for a positive resist. During this development, a polymer mask is created on the sample which provides a base for further processing, such as by depositing metal patterns or etching using chemical or plasma etching.

The oldest lithography method used in microfabrication is photolithography, where patterns are transferred to the chip using an UV sensitive polymer[26]. In this method, a laser is used to transfer the desired pattern used onto a photomask, which consists of a chromium-covered glass plate. During exposure, the photomask is placed between the chip and the light source. The opague, chromium covered parts act as a barrier, while the light unhindered travels through the clear areas of the glass. This method is fast and effective, but is hindered by the diffraction limit, meaning that very fine details can't be defined using this method.

An alternative to photolithography is electron-beam lithography (EBL), where a beam of energetic electrons are focused down, writing out the pattern[22]. This method has an extremely high resolution, with the lower limit for the ELIONIX ELS-F125 being 7nm. A set of beam deflectors controls the course of the beam, enabling writing of arbitrary patterns without a physical mask. However, the single electron beam results in a long write time for large and complex patterns. In the EBL, a ray of highly energetic electrons are shot out from an electron beam gun. A schematic can be seen in figure 5.1a. On the way, it passes through several focusing lenses, only the last of which are shown on the figure. A set of beam blankers are used to blank the beam during stage movement and during realigning of the electron beam spot by the deflectors. The light passes through an aperture, which reduces the beam spot size. The position of the beam on the sample is controlled by a set of beam deflectors, just before the final focusing lens focuses the beam to a small spot on the substrate[22].

In the EBL, the pattern is divided into a series of writing fields, which in the recipes used for this project has a size of 500 μm $\times$ 500 μm. In each writing field, the pattern is sub-divided into smaller polygons. The EBL machine will move the stage to the position of one writing field, and then expose the pattern to the electron beam polygon by polygon by moving the beam with the deflectors, before moving the stage to the position of the next writing field. While the stage position is measured extremely precise using interferometers, the seams between the writing fields are not guaranteed to have perfect alignment. If possible, the pattern should be designed in a way that allows for seamless fabrication, meaning that the devices are organized in islands that can be entirely contained within one writing field and no device will be positioned on two writing fields.

Positive resists typically consists of long polymer chains. During exposure, collisions between the resist and the energetic electrons breaks up the bonds in the chain, turning the long polymer into smaller pieces. This makes the former very insoluble resist highly soluble in places where it has been exposed. Conversely, negative resists typically consists of smaller polymers which forms crosslinks during exposure. After exposure, the sample is developed by immersing it in a solvent which dissolves the polymer fragments for a positive resist, or the non-crosslinked molecules for a negative resist. The size of molecules dissolved by the developer depends on the time the sample is immersed and the strength of the developer[3].

The dose received during exposure is measured in charge per area, and describes how many energetic electrons have hit the resist during exposure. Too low dose means that the resist will

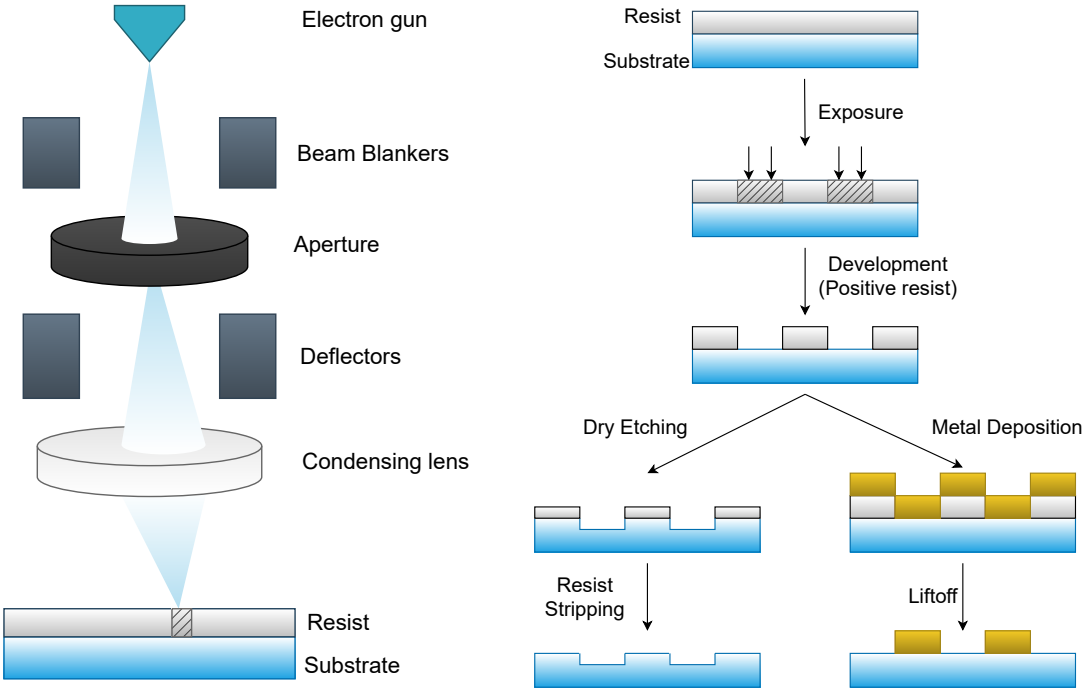

(a) Schematic of electron-beam lithography (b) Procedure for metal deposition and dry etching

Figure 5.1: Schematics showing e-beam lithography and fabrication procedures

not be fully penetrated by the electrons. During development, an under-exposed resist will not act properly. For a positive resist, the resist will not be stripped fully away during development, while a negative resist might have some or all of the exposed pattern stripped away during development. Meanwhile, too high a dose means that the surrounding areas might receive dose as well, leading to potential collapse of fine features[22].

The main effect limiting the resolution of EBL exposure is due to scattering effects. Forward scattering is due to electrons being deflected by the polymers in the resist while it is passing through. This broadens the beam, lowering the resolution. A higher acceleration voltage will lead to the electrons having greater energies, letting them pass through the resist unhindered, leading to less scattering, and thus a more precise pattern. Backscattering is due to electrons in the substrate undergoing a series of large-angle reflection that scatters them back into the resist. This leads to a phenomenon known as the proximity effect where the scattered electrons interact with the surrounding areas on the sample rather than the exact point where they are applied[22]. An electron from the beam applied to write one feature can thus end up causing exposure at the position of another feature, leading to overexposure in areas with high density of features. This can be corrected by using a software such as BEAMFOX where the actual dose to be applied to each position is recalculated by taking nearby exposed areas into account, finding the actual dose necessary to get the desired dose after the proximity effect is accounted for.

For the second and third exposure, precise alignment with the former layers is of utmost importance, and a set of crosses laid down during the first exposure are used for alignment. In order to check whether the alignment is precise, a set of Vernier scales are defined at several

positions on the chip,, enabling to very precisely see the alignment between the two layers.

5.2 Metal Evaporation

Metal strips on integrated circuits are often used for electrodes, allowing for the application of electric fields on the circuit. For the novel device described in this thesis, metal strips are placed along cantilever waveguides, leading to a bending. The placement is done using a metalization/liftoff procedure, where after the exposure and development, the sample is coated in a thin metal film. Removing the resist also removes the metal film on top of it, leaving only the metal film on the positions where the resist was removed.

For the placement of the metal strips, the chip is spincoated with a CSAR13 positive resist, and exposed using e-beam exposure. Initial fabrication used a $200\,\mathrm{uC/cm^2}$ dose, but this lead to errors in the metal deposition, causing imperfections visible on an optical microscope. While the source of these imperfections were not found, increasing the dose to $300\,\mathrm{uC/cm^2}$ for the subsequent chips removed this phenomena.

After development, the chip is descummed using oxygen plasma. This burns residual polymer on the sample surface, ensuring that the metal will stick to the substrate. The metal is deposited on the wafer using physical vapour deposition (PVD). The sample is fixed to a sample holder, which is loaded upside down into the evaporation chamber. The chamber is pumped down to a vacuum of approx. 10^{-7} mbar. Following this the desired metal, which is kept in a crucible inside the evaporation chamber, is bombarded with electrons at high energies. This, combined with the vacuuum in the chamber, creates a metal vapor, which coats the entire sample and sample holder with a thin film. Since the metal is evaporated by energy transfer from the electron beam rather than heat, the evaporation chamber can hold more than one crucible. The metal layer is 180 nm thick in total, consisting of 10 nm Cr, 160 nm Ni and 10 nm Au.

During liftoff, the sample is immersed in 1,3-dioxolane at room temperature. By gently blowing at the sample with a pippette, the resist will lift off, and the metal laying on the resist with it, leaving only the metal pattern on the GaAs. A schematic showing the process of metal deposition using a positive resist can be seen to the left in figure 5.1b

5.3 Etching

Metal deposition creates metal patterns on the substrate surface. Besides this, methods for carving patterns into the GaAs membrane itself exist. This includes shallow etching, where features are carved partways into the GaAs membrane, and deep etching, where all of the substrate is carved through. For deep etchings, the underlying sacificial layer can afterwards be etched away chemically by immersing the sample into caustic chemicals that are capable of dissolving the sacrificial layer but not the main substrate. This is what creates the suspended waveguides.

Two main types of etching exist. In dry etching, the sample surface is bombarded with high-energy gasses and plasmas, which carve out features with a combination of chemical and physical processes. In wet etching, the sample is immersed into a corrosive fluid, and the exposed areas etched away chemically. Wet and dry etching have different advantages and disadvantages. Due to the different physical processes, the etch profiles are different, with physical etching generally giving straight edges, while wet etching giving curved edges. Wet etching have the additional advantage that it can be carried out in relatively low-cost laboratories, while dry etching require expensive and complicated machinery. Furthermore, wet etching can be highly selective, meaning that the solvent can be chosen to etch the desired membrane without etching the surrounding material. When fabricating the samples used for this thesis, dry etching is used for defining the waveguides in the GaAs layer, whil HF was used for wet etching due to having a 10:1 selectivity

for respectively AlGaAs and GaAs[3]. This allows for the use of HF to etch away the AlGaAs sacrificial layer, suspending the waveguides and freeing the cantilevers.

In general, dry etching create more anisotropic etches, whereas wet etching creates isotopic etching. Here, isotropy is defined as the ratio of vertical etching to horizontal etching. A highly anisotropic etching creates even walls, while isotropic etching creates a rounded wall.

5.3.1 Dry Etching

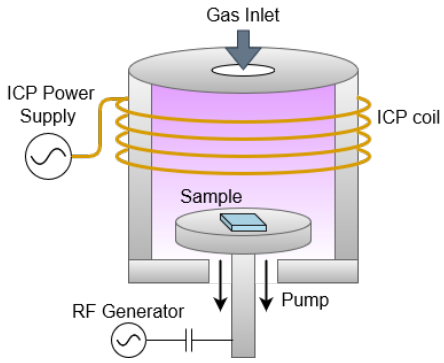

Figure 5.2: Schematic of an ICP machine.

For the second step, the waveguides and cantilevers are defined in the GaAs using dry etching. The etching method is a form of Reactive Ion Etching (RIE), where a source gas is dissociated into a plasma using a Radio Frequency (RF) power supply. This plasma contains reactive radicals and ions, which are bombarded down on the sample by the same RF field.

Since the same power supply is used to control both plasma formation and direction and acceleration of the ions, the degree of plasma dissociation and the kinetic energies of the ions cannot be independently controlled. As an alternative, the power supply can be separated, with one generating the plasma and the second one providing the RF field that controls the acceleration of the ions. In this method, a coil is used to inductively generate the plasma, and because of that the technique is named Inductively Coupled Plasma (ICP). Several different methods of dry etching for the sample was tested, with the final method used being RIE etching using the gases BCl_3 and Ar

During dry etching, the electrically charged plasma is guided at high velocities directly down to the chip. Here, two separate mechanisms work together to etch the sample. Physically, where the ions knocks the upper layers of the sample loose in a process called sputtering, and chemically, where the ions react with the sample. Sputtering is dominant at low pressures and high voltages where the ions hit the sample with a very high velocity and create a very anisotropic etching profile with inclined walls, but also gives a higher risk of damaging the substrate. Chemical etching is dominant for high pressures and low voltages and gives a sloping, highly isotropic etch profile. Balancing the physical and chemical etching processes are tantamount to getting an even etching with straight walls.

Ramping up the power of the ICP coil gives stronger chemical etching, while ramping up the RF power gives stronger physical etching. Being able to separately control the contributions from chemical and physical etching enables a degree of control over the etching profile which is important especially for narrow, deep features.

During the procedure, the etching depth can be measured by measuring the reflected light from a laser beam on positioned on a large $200\mu\text{m} \times 200\mu\text{m}$ square exposed in the resist. The reflectance

changes depending on the thickness of the substrate, and noticeable changes when shifting from the GaAs substrate to the AlGaAs sacrificial layer. The reflectance pattern for the wished-for etch depth has been simulated in advance, and the etching is discontinued once the the wished-for reflectance pattern is reached.

5.3.2 Wet Etching

The wet etching is carried out using Hydrogen Flouride (HF), which capable of etching AlGaAs but not GaAs. During the wet etching, the sacrificial AlGaAs layer is removed along the features etched in the GaAs during the dry etching. In comparison with RIE etching, where the anisotropic process creates straight walls along the etching, the isotropic chemical process of HF etching creates an undercut, meaning that the etching spreads to beneath the GaAs. This suspends the waveguides and releases the cantilevers. After the etching, the sample should be cleaned of HF by submerging it in several rounds of Milli-Q (MQ) water, before being moved to isopropane alcohol (IPA). Due to the fragility of the suspended waveguides and bent cantilevers, the sample should not be allowed to airdry after the undercut is performed.

Micro-and nanodevices, especially those with undercuts or cantilevers, are fragile, and will collapse if allowed to airdry due to the surface tension of the evaporating solvent. Instead, critical point drying (CPD), where the sample is dried by adjusting the temperature and pressure in the machine to "go around" the critical point of the solvent. At temperatures and pressures beyond this point, the distinction between the liquid and gaseous phases vanish, and the evaporation will be continuous rather than discrete.

During the CPD process, the solvent (such as ethanol, acetone or IPA) is washed away with several rounds of pressurized carbon dioxide. Carbon dioxide, whose critical point lies at $T = 304.25$K and $7.39MPa$ is the solvent of choice for CPD, since it is non-toxic, is relatively inert in its supercritical state, and reaches the critical point at a low temperature, avoiding heat damage to the sample. After several rounds of CO_2 washes, the temperature and the pressure are slowly adjusted to go around the critical point of carbon dioxide. Extreme care must be taken while working with HF. While it is a relative weak acid in the case of a spill, the corrosion of the outer layers of the skin caused by the H+ ions will allow the extremely toxic flouride ions F- to penetrate deeply into the body.

5.4 Summary

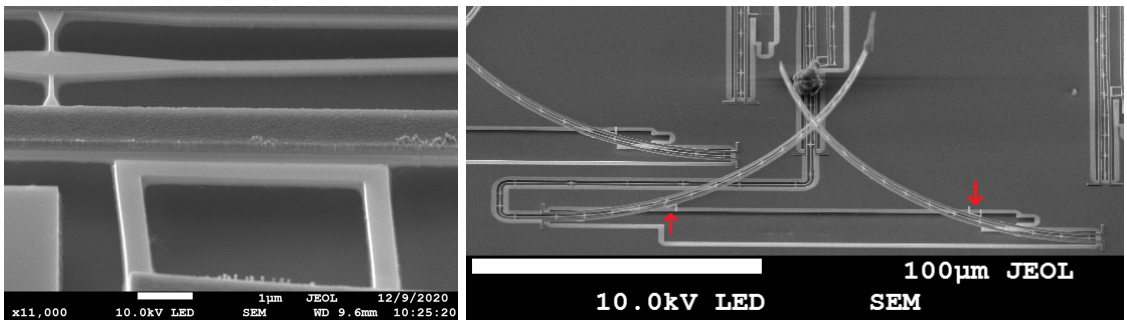

(a) Incomplete etch (b) Raised waveguides

Several challenges were met during the fabrication step. First of all, the CPD broke down suddenly and unexpectedly. This not only destroyed the chip currently undergoing CPD, but also necessitated using the CPD machine at the CFIM, or Core Facility for Integrated Microscopy. The

travel to and from CFIM required taking a lot of care during transport. Due to the CFIM being a biological facility and having different standards of cleanliness than the cleanroom and fabrication facilities at HCØ, contamination from the CPD was also an issue.

The first chip fabricated using the CPD at CFIM has the waveguide collapsed. Using the SEM, it was possible to see how the surface structure and edges of both the GaAs layer and the metal strips were extremely rough, and how the surface of the GaAs wafer and GaAs substrate under the sacrificial AlGaAs layer seemed almost porous. A possible reason for this effect is that after exposure amd development of the negative epoxy resist, the residual resist is removed by descumming in the ICP for 300 seconds. Since ICP consists of energetically ions bombarded into the wafer surface at a high speed, this could possibly have led to damage to the surface. Furthermore, on one of the fabricated chips, the locks, which in the finished structure keeps the waveguide in an upright position, were not properly etched away from the waveguide beside it. The distance between the edge of the lock and the waveguide lying beside it is very small at only 200 nm. A very narrow and deep etch is thus needed here. It can be seen on the photos how the undercut is fulfilled on the device, meaning that the AlGaAs sacrificial layer is etched through, but the 160 nm thick GaAs layer at the top is not etched through. A few waveguides on this chip were, however, freed during the undercut. Those devices can be seen in figure. However, the waveguides freed were not because the trench between the lock and the neighbouring waveguide were fully etched, but because the waveguide broke free of the lock.

Also, even for the waveguides where the lock kept the waveguide down, the intrinsic stress mismatch between the layers were strong enough for the device to tear the cantilever tethers apart, allowing the Ni/GaAs cantilever not connected to the lock to rise, through collapse of the waveguide meant that the cantilever did not go as high as it otherwise could have done. The cantilevers that tore themeselves apart were the one that didn't have epoxy tips, because the epoxy tip kept it together.

Figure 5.4 shows an example of a simple device using the bent cantilever waveguides. Each of these devices consists of two sets of hooked-together cantilevers, where the two cantilevers containing the couplers are connected by a suspended GaAs waveguide. On figures 5.5a and 5.5b, the epoxy-covered tip of the waveguide can be seen. The epoxy acts as spot-size converters[33], allowing for easy in- and outcoupling. The larger size of epoxy compared to the tip allows the waveguide to be in contact with more of the beam spot, resulting in higher efficiency.

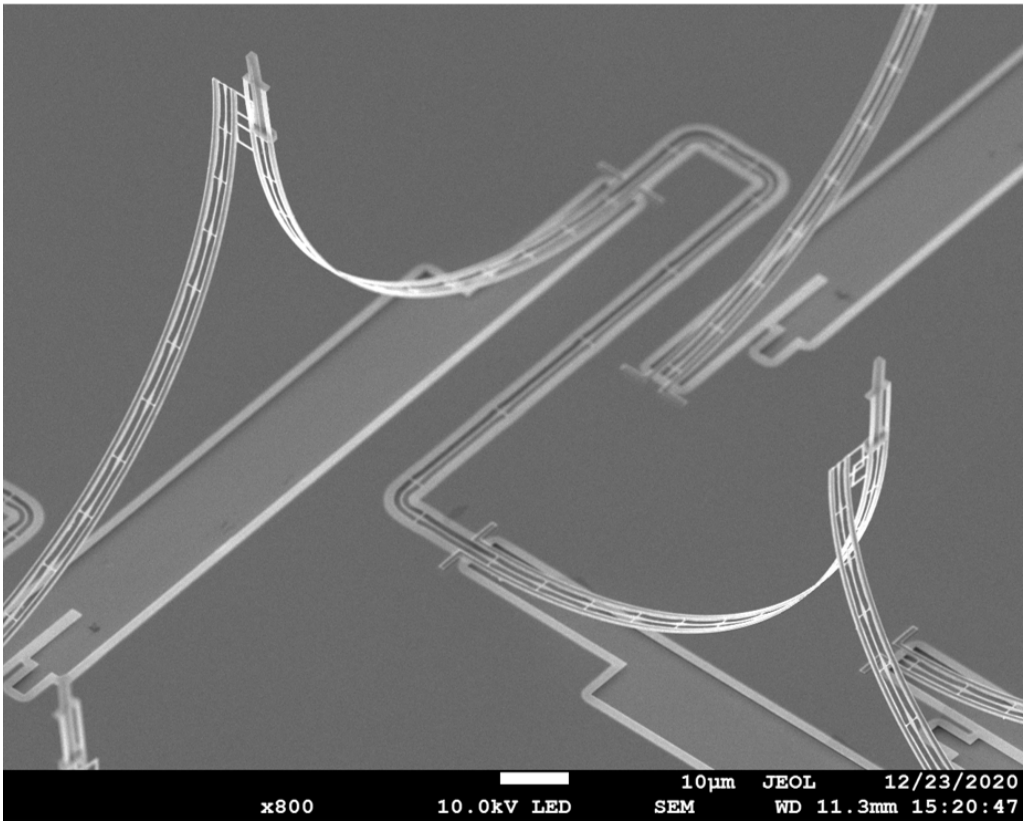

Figure 5.4: SEM photo of the bent cantilever waveguides. Image was taken by Zhe Liu

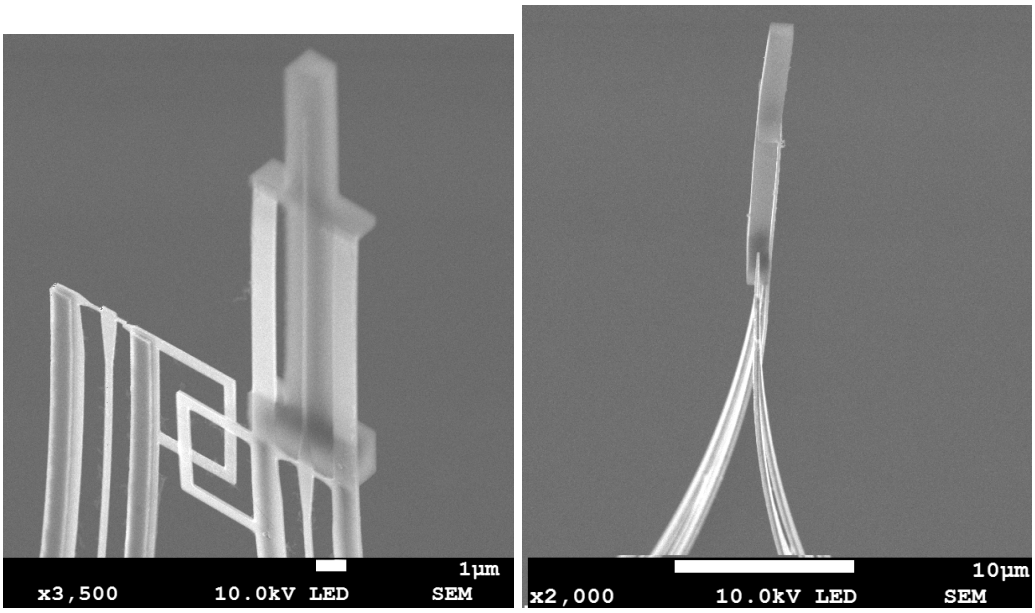

(a) SEM photo of the epoxy clad tip of the bent waveguide. The tapered GaAs tip can be seen inside the epoxy. Image was taken by Zhe Liu

(b) SEM photo of the epoxy tip seen from the side. Note the slight curvature of the epoxy-clad tip - it is not completely vertical.Image was taken by Zhe Liu

Figure 5.5: SEM photos showing the epoxy clad tip of the curved cantilever waveguide

Chapter 6

Characterization of the curved cantilever waveguide

In this chapter, the experimental characterization of the strained cantilever waveguide is described. Two modes, one corresponding to the Transverse Electric (TE), and one corresponding to the Transverse Magnetic (TM) were identified. Using a SuperK supercontinuum laser spanning an extremely wide range of wavelengths, the wavelength-dependent transmittivity is measured at room and cryogenic temperatures in a wavelength interval spanning the interval $850 - 1170$ nm, with both bounds being set by technical limitations. Measurements for the TE mode were also taken at temperatures in the range 10-293 K, and used to explain the behavior of the waveguide.

6.1 Experimental Setup for device characterization

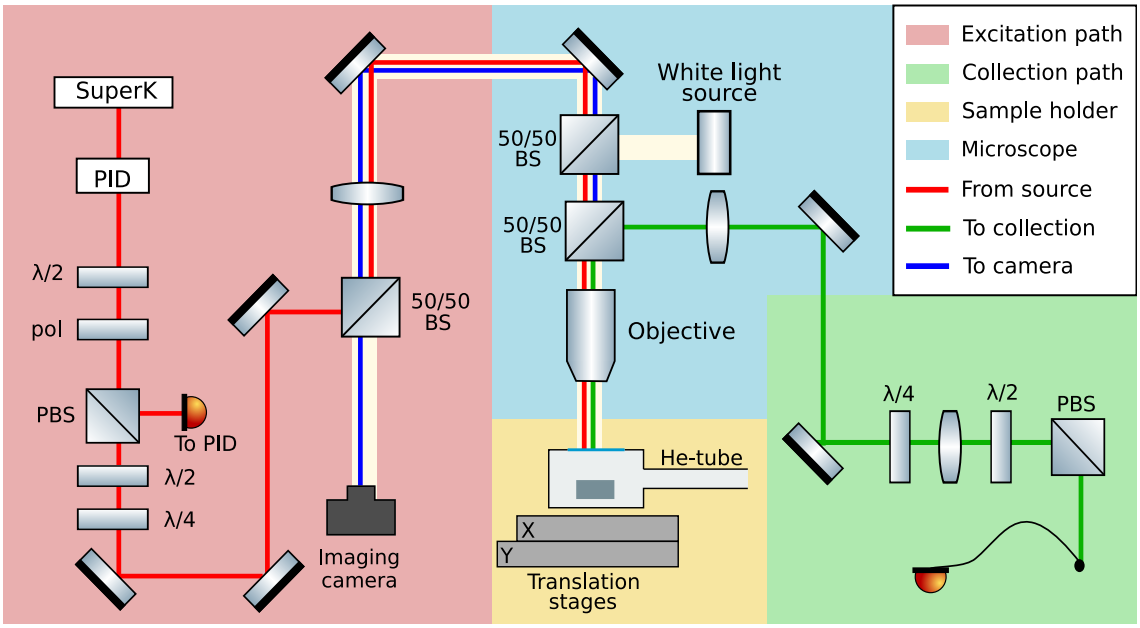

Figure 6.1: The optical setup.

Device	A13	A41	C41
Radius of curvature [μm]	78.08	78.08	78.08
Tether distance [μm]	10	15	15
Epoxy tips	Yes	Yes	No

Table 6.1: Parameters for the devices under characterization.

The sample was glued to a chip carrier and placed in a cryostat A CTL laser was used to calibrate to the TE and TM modes, while a SuperK supercontinuum laser was used to give a wide spectrum for the broadband transmittivity measurements. The power of the laser was kept constant using a PID controller.

In comparison to shallow-etch grating couplers, who allow transmission of only TE modes[38], the tips of the cantilever waveguides couple to TE and TM modes both. Since the TE and TM modes couple differently to the waveguide, it was a wish to measure the transmission spectrums for respectively the TE and the TM modes. The TE and TM modes were found by aligning a set of a half-wave plate (HWP) and quarter-wave plate (QWP), which is placed on both the excitation and the collection path. A challenge was present in identifying the TE-like and TM-like modes of the device, since no shallow-etch grating was present on the chip. Instead, a set of shallow-etch gratings present on another chip glued to the same chip carrier was used to align the chips. The translation stages was moved until the camera focused on one of the sets of shallow etched gratings, and the excitation laser was moved to one of the SEG couplers. The integrated transmission, measured by taking the sum of the pixels of the light spot on the SEG at the other end, was then measured by adjusting the HWP at the desired angle, and then finding the orientation of the QWP that gave respectively the minimum and the maximum value, before moving the HWP $5 - 10^\circ$ and finding the QWP angle that gave the minimum and maximum value at the new HWP angle. The combination of HWP and QWP that gave respectively the minimum and maximum total value were hereafter defined as respectively the TM and TE modes of the excitation.

It was sadly not possible to align the HWP and QWP on the collection path using by coupling the source to the collection path, since the fiber between the source and the collection path did not preserve the polarization of the beam, leading to a slow polarization drift. Since a polarizing beam-splitter were placed in the collection path after the HWP and QWP, the polarization drift caused a strong variation in measured intensity, meaning that the measured intensities could not be properly compared. Instead, the excitation path was adjusted to the TE mode, and the collection and excitation path aligned to two connected SEGs. The QWP orientations that gave the maximum and minimum transmission through the device for a series of different HWP angles was then measured using a spectrometer, and the HWP and QWP combinations that gave the total maximum and minimum transmission were termed the TE and TM modes of the collection.

6.2 Efficiency measurements

With the calibration of the path that gave the TE and TM modes identified, the characterization of the transmittivity of the devices could be carried out with good control of the polarization. Most of the measurements were carried out on one device, termed A13, but other measurements were taken on devices A41 and C41. The parameters for each of these devices can be seen on table 6.1

The transmission through the device was measured for the TE and TM modes, after which the excitation and collection path were focused on the same spot, and spectrums were taken for the TE, TM modes, getting the reflection from bulk and the reflection from the tips, while focusing on respectively the bulk surface and the end of the epoxy tips.

Once the spectrums are taken, the efficiency for the TE and TM modes can be calculated by

$$\eta = \frac{I_{transmission}}{I_{bulk} \cdot R_{GaAs}}. \tag{6.1}$$

The used reflectance $R_{GaAs} = 0.3$ is valid for the investigated wavelengths[1].

6.3 Characterization of the devices

6.4 Transmission efficiency

The figure was characterized both at room temperature (293 K) and at cryogenic temperature (10 K), where it was cooled down using a Helium flow cryostate. During the cooling, the devices showed themselves to be robust, working the same after being cooled down to and back to room temperature several times. In figure 6.2, the efficiencies for the TE and TM modes at respectively room temperature and 10 K can be seen.

The raw efficiency is very low compared to other types of couplers. One type of loss that needs to be accounted for is propagation loss, which is high due to the surface roughness of the waveguide[35]. This loss is of the order of magnitude of 7 dB/mm. With the device having a length of $L = 435\ \mu$m, this means that the device has a loss of 3.05 dB. In figure 6.2 the efficiency corrected for propagation loss is shown. Accounting for propagation losses thus doubles the efficiency, although it is still much lower than other types of couplers[38].

6.5 Bandwidth and cutoff

When taking the measurements, it was noticed that the TE and TM mode both had a powerful temperature-dependent wavelength cutoff, as can be seen on figure **??**. This cutoff was an extremely surprising find, and a large part of the work on this thesis was spent trying to explain it.

The cutoff, which at room temperature was found to be 935 nm for the TE mode and 905 nm for the TM mode, and at cryogenic temperature $T = 10\,\text{K}$ was 880 nm for the TE mode and 850 nm for the TM mode. An initial theory is that it was caused by the epoxy tip. This, however, would not agree with the previous simulations of the wavelength-dependent transmittivity through the epoxy[33]. Room-temperature measurements on a device without the epoxy coating on the top also showed the same cutoff as the epoxy-coated version, as can be seen in figure 6.3. Furthermore, as can be seen in table 6.1 that the used devices have different tether distances, it can also be ruled out that tether distance has a large influence on the cutoff. The variation in strength of the transmission for different wavelengths for the different devices is likely because the transmission through the device is extremely sensitive to changes in alignment, and thus miniscule changes in relative positioning between the different experiments have likely led to the variation in the overall shape of the transmission spectrums.

The source of the rapid oscillations in the spectrum intensity with period 6 nm was investigated. It most likely originates in the SuperK setup, since it showed up when sending light directly from the PID to the spectrometer, and since the spectrum for a CTL sweep showed a different pattern for oscillation.

While the efficiency is low, as mentioned in the previous section, and the mysterious cutoff prevents transmission of light with low wavelengths, the coupler shows an extremely large bandwidth, with the shown measurements having FWHM bandwidths $FWHM_{TM,10\,\text{K}} = 180\,\text{nm}$, $FWHM_{TM,293\,\text{K}} = 109.8\,\text{nm}$, $FWHM_{TE,293\,\text{K}} > 81\,\text{nm}$, $FWHM_{TE,10\,\text{K}} > 159\,\text{nm}$. For the TE mode, it can't be known how large the bandwidth is, since the laboratory this thesis was carried out in did not have a detector that could detect photons with wavelengths above 1070 nm. The

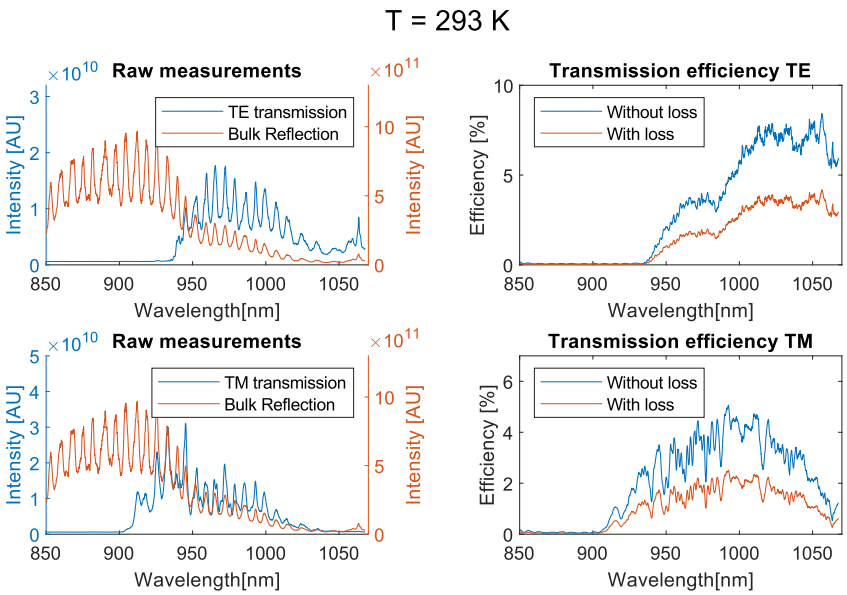

(a) Efficiency at room temperature for the TE and TM modes.

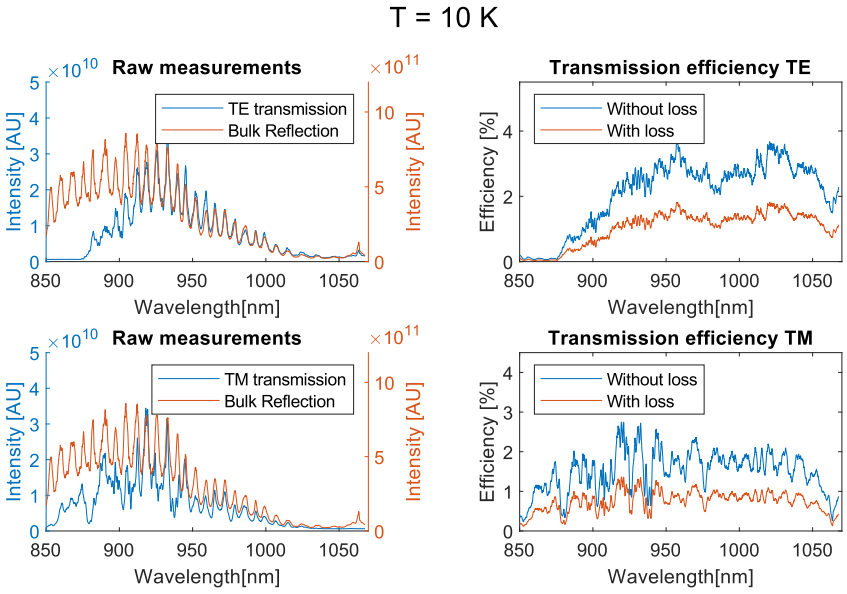

(b) Efficiency at room temperature for the TE and TM modes.

Figure 6.2: Efficiencies for the measurements at respectively 10K and 293 K. Note how the plots containing the raw measurements each have two y-axes. For the plots containing the transmission efficiencies, "With loss" is the percentage of the light that is transmitted through the waveguide while "Without loss" is what the transmission would have been if the scattering loss estimated at 7 dB/mm had not been there.

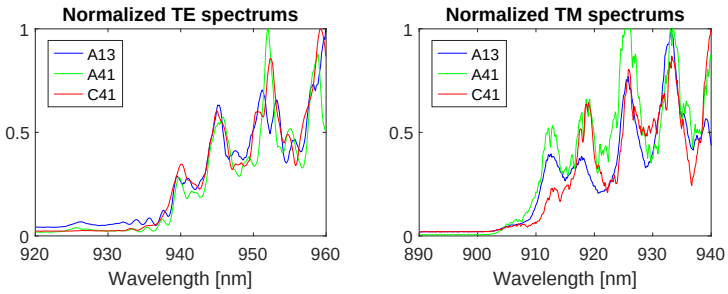

Figure 6.3: The transmission spectrums for different devices.

dip in intensity for wavelengths above 920 nm is due to the intensity of the superK laser having a dip in that interval, followed by an abrupt spike at 950 nm

6.6 Investigation of temperature dependence of transmittivity

In order to shine light on the temperature dependence of the behavior if the device, the TE spectrum was measured over a wide range of temperature. This was done by gradually cooling down the device, by controlling the amount of Helium being pumped through, while carrying out an on-going alignment of the focus and the optical path. There was no interface allowing the temperature to be automatically read by the script taking the measurement and instead the measurement was logged manually for different temperatures. However, especially at temperatures below 100 K, the cooling effect was hard to control, and the measurement was taken by executing the script when the temperature hit exactly the desired point.

In total, 23 measurements were gathered at temperatures ranging from 10-290 K. In figure 6.4, the spectrum for measurements taken at seven different temperatures can be seen. The reason for the large variation in the intensity of the measurement is that since the device had to be continually realigned while cooling down, the hard-to-control cooling effect sometimes necessitated taking the measurement with sub-optimal alignment.

It can be seen clearly in figure 6.4 how the cutoff very strongly correlates with the temperature. In an attempt to explain the temperature-dependence of the cutoff it was compared to the temperature dependence of the GaAs bandgap, which GaAs without strain and external electric fields can be modelled as [4]

$$E_g(T) = 1.519\,\text{eV} - \frac{5.405 \cdot 10^{-4}\,\text{eV/K} \cdot T^2}{T + 204\,\text{K}}. \tag{6.2}$$

If light is conducted through a semiconductor waveguide, photons with energies above the bandgap energy will be absorbed. The cutoff wavelength, which was compared to the temperature-dependent GaAs bandgap, was estimated by identifying the wavelength at which the photons begin to be transmitted. Then the data was fitted to the model.

$$E_g(T) = \beta + \frac{\alpha \cdot 10^{-4} \cdot T^2}{T + 204K} \tag{6.3}$$

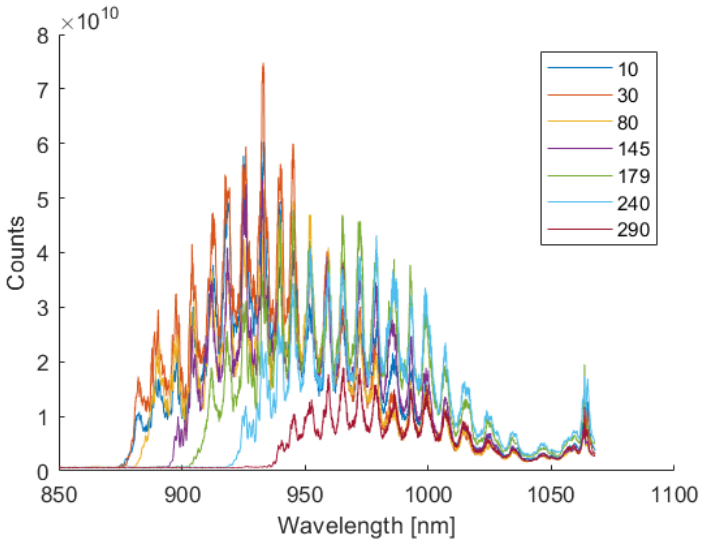

Figure 6.4

The parameters, with 95% confidence intervals, were found to be respectively

$$\beta = 1.420 \pm 0.001 \text{ eV}, \quad \alpha = -5.33 \pm 0.11 \cdot 10^{-4} \text{ eV/K} \tag{6.4}$$

Since $\alpha_{fit} = -5.33 \cdot 10^{-4}$ eV/K $\pm\, 0.105 \cdot 10^{-4}$ eV/K and $\alpha_{theory} = 5.405 \cdot 10^{-4}$ eV/K, the theoretical slope is thus within the bounds of the fitted slope, while the offset β has a difference of 0.1 between fit and theoretical value.

The uncertainties on the fit, however, does not take measurement uncertainties into account, and is instead purely a metric of how well the data can be modelled by the fit. The measurement was only taken once for each temperature, and thus the normal method of identifying random errors by the means of calculating the standard deviation could not be found. Instead, measurement uncertainties must be estimated. For these calculations, the uncertainty on the cutoff wavelength is estimated at 2 nm, while the measurement uncertainty on the temperature is estimated at 1 K.

For the formula

$$E_g = \beta + \frac{\alpha \cdot 10^{-4} \cdot T^2}{T + 204 \text{ K}} \text{ [eV]} \tag{6.5}$$

With uncertainties both on λ and T, the total uncertainty can be found by propagation of errors

$$\sigma_E^{eff} = \sqrt{\sigma_E^2 + \left(\frac{\partial E}{\partial T}\right)^2 \sigma_T^2} \tag{6.6}$$

Calculating

$$\frac{\partial E}{\partial T} = \frac{\alpha T}{204 \text{ K} + T}\left(2 - \frac{T}{204 \text{ K} + T}\right) \tag{6.7}$$

Similarly, the uncertainty on the bandgap due to the estimated uncertainty on the wavelength

$$\sigma_E = \frac{hc}{\lambda^2}\sigma_\lambda \tag{6.8}$$

The error can thus

$$\sigma_E^{eff}(T,\lambda) = \sqrt{\left(\frac{hc}{\lambda^2}\sigma_\lambda\right)^2 + \left(\frac{\alpha T}{204\,\mathrm{K}+T}\left(2-\frac{T}{204\,\mathrm{K}+T}\right)\right)^2\sigma_T^2} \tag{6.9}$$

Plugging in the fit values $\alpha = -5.33\cdot10^{-4}\,\mathrm{eV/K}$, $\beta = 1.420\,\mathrm{eV}$ and the uncertainties $\sigma_\lambda = 2\,\mathrm{nm}$, $\sigma_T = 1\,\mathrm{K}$.

The chi-squared value can then be found

$$\chi^2 = \sum_i \frac{(E_i - E_i(T))^2}{\sigma_i^2} = 2.95 \tag{6.10}$$

From this, the reduced chi square can be found by dividing the χ^2 with the degrees of freedom, which is the number of measurements minus the number of fit parameters. With 23 measurements and 2 fit parameters

$$\chi^2_{red} = \frac{\chi^2}{23-2} = 0.1406 \tag{6.11}$$

This identified χ^2_{red} is very low, and means that the uncertainties probably have been overestimated. This estimate does not, however, take systematic errors into account.

A comparison of the fits and the theoretical value for the GaAs bandgap is shown in figure 6.5. It can be seen that while the slope of the model is very close to the slope for the theoretical bandgap, there is a temperature-independent offset of $E_{change} \approx 0.1\,\mathrm{eV}$. In the next section, the hypothesis that this offset originates ifrom a strain-induced bandgap shift will be investigated.

6.7 Discussion of measured bandgap change

The theoretical value for the GaAs absorption edge is $\lambda_{10K} = 817\mathrm{nm}$ at 10 K and $\lambda_{293K} = 871\mathrm{nm}$ at 293 K. Comparing the theoretical bandgap to the measured cutoff for the manual set of parameters, the observed bandgap shift becomes

$$\Delta\lambda_{TE,293K} = 67\,\mathrm{nm}, \quad \Delta\lambda_{TM,293K} = 39\,\mathrm{nm} \tag{6.12}$$

$$\Delta\lambda_{TE,10K} = 63\,\mathrm{nm}, \quad \Delta\lambda_{TM,10K} = 33\,\mathrm{nm} \tag{6.13}$$

Or in electron-volt

$$\Delta E_{TE,293K} = -0.1017\,\mathrm{eV}, \quad \Delta E_{TM,293K} = -0.0610\,\mathrm{eV} \tag{6.14}$$

$$\Delta E_{TE,10K} = -0.1076\,\mathrm{eV}, \quad \Delta E_{TM,10K} = -0.0578\,\mathrm{eV}, \tag{6.15}$$

Referring to the 4×4 Pikus-Bir Hamiltonian, which is described in chapter 3, the analytical solution for the band gap change due to strain is

$$\Delta E_{1/2} = (a_c + a_v)\mathrm{Tr}(\epsilon) \mp \sqrt{|Q_\epsilon|^2 + |R_\epsilon|^2 + |S_\epsilon|^2} \tag{6.16}$$

Here band 1 and 2 refers to the fact that in the presence of non-hydrostatic or biaxial normal strain, the HH and LH bands will hybridize. Band 1 and 2 are the new, now non-degenerate, eigenstates of the strained material. This can be separated into two parts,

$$E_{shift} = (a_c + a_v)\mathrm{Tr}(\epsilon), \quad E_{split} = \sqrt{|Q_\epsilon|^2 + |R_\epsilon|^2 + |S_\epsilon|^2} \tag{6.17}$$

With the energy shifts for the two different modes being measured, the shift and split of energy can be found

$$E_{shift} = \frac{\Delta E_{TE} + \Delta E_{TM}}{2}, \quad E_{split} = \frac{|\Delta E_{TE} - \Delta E_{TM}|}{2}, \tag{6.18}$$

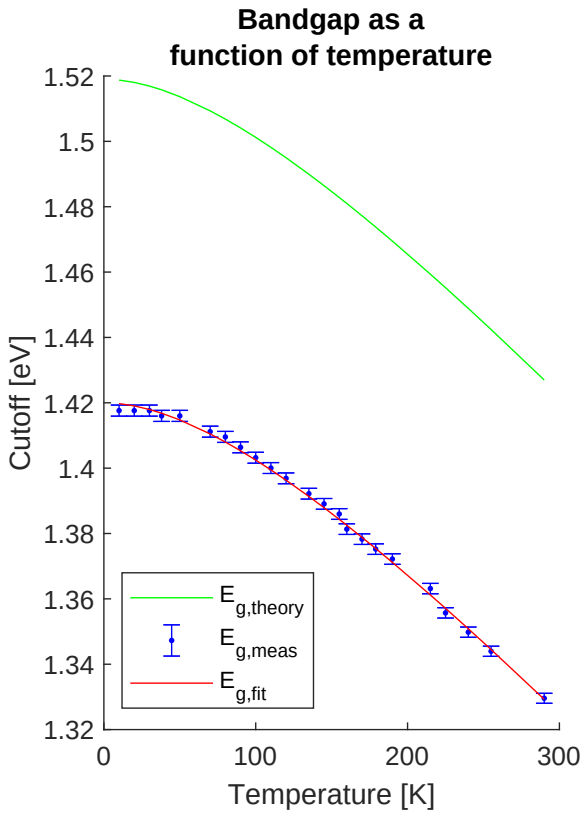

Figure 6.5: The temperature dependent band-gap of GaAs. Shown is the theoretical value, the measurements of the cutoff, and the fit. For ease of reading, the entire propagated error is placed on the measured value, when it most correctly should be split between the fit and the measurement.

Assuming that all the band gap shift comes from strain, the two terms can be calculated for the results at respectively 10 K and 293 K

$$\begin{aligned} E_{split,293K} &= 0.0407\,\text{eV} = 2\sqrt{|Q_\epsilon|^2 + |R_\epsilon|^2 + |S_\epsilon|^2} \\ E_{split,10K} &= 0.0508\,\text{eV} = 2\sqrt{|Q_\epsilon|^2 + |R_\epsilon|^2 + |S_\epsilon|^2} \end{aligned} \tag{6.19}$$

$$\begin{aligned} E_{shift,293K} &= -0.0814\,\text{eV} = (a_c + a_v)\text{Tr}(\epsilon) \\ E_{shift,10K} &= -0.0832\,\text{eV} = (a_c + a_v)\text{Tr}(\epsilon) \end{aligned} \tag{6.20}$$

Equations 6.19 and 6.20 make up two equations with 6 variables, from the 6 independent components of the strain tensor. It is assumed, due to the material symmetry of the cantilever, that the following simplifications will always hold.

$$\epsilon_{xx} = \epsilon_{yy}, |\epsilon_{yz}| = |\epsilon_{xz}| \tag{6.21}$$

Furthermore, for simplifications sake, I am assuming that $\epsilon_{yz} = \epsilon_{xz} = 0$, meaning that $S_\epsilon = 0$. Using this and that $a_c = -7.17$ eV, $a_v = -1.16$ eV, $b = -2$ eV, $a_v = -1.16$ eV, $b = -2$ eV, $d = -4.8$ eV [32]

$$\Delta E_{1/2} = -8.33\,\text{eV}(2\epsilon_{xx} + \epsilon_{zz})(\epsilon) \mp \sqrt{(-2\,\text{eV}(\epsilon_{xx} - \epsilon_{zz})^2 + (-4.8\,\text{eV}d\epsilon_{xy})^2} \tag{6.22}$$

This reduces the number of unknowns in the system of equations to 3, which does still not allow for exact solutions. However, by recalling that the strain in the cantilever comes as a result of stress, either intrinsic or applied, a potential theoretical solution for the strain can be calculated using by assuming simple models containing one or two types of stress in the system and then solving for those unknowns.

6.7.1 Analyzing for strain caused by uniaxial shear stress

A possible cause of the strain in the waveguide is induced by uniaxial shear stress. The stress tensor in this case can be found to be $\sigma_{xx} = \sigma_{yy} = \sigma_{xy} = T/2$ and $\sigma_{zz} = \sigma_{yz} = \sigma_{zx} = 0$.[32] From here, the components of the strain tensor can be obtained using the compliance matrix from equation 3.11.

$$\epsilon_{xx} = \epsilon_{yy} = \frac{S_{11} + S_{12}}{2}T \tag{6.23}$$

$$\epsilon_{zz} = S_{12}T \tag{6.24}$$

$$2\epsilon_{xy} = \frac{S_{44}}{2}T \tag{6.25}$$

For strain induced by uniaxial shear stress, the relationship between the strain terms is thus

$$\epsilon_{zz} = \frac{2S_{12}}{S_{11} + S_{12}}\epsilon_{xx} = -1.006\epsilon_{xx} \quad \epsilon_{xy} = \frac{S_{44}}{2(S_{11} + S_{12})}\epsilon_{xx} = 1.106\epsilon_{xx} \tag{6.26}$$

Recalling that, in chapter 4, it was found that the the following general relation for the identified strains hold $\epsilon_{xx} = \epsilon_{yy} \approx -\epsilon_{zz} \approx \frac{1}{1.1}\epsilon_{xy}$.

This also means for band gap shifts caused by strain from uniaxial shear stress, there will be a constant relationship between the energy split and the energy shift. Using that, for GaAs,

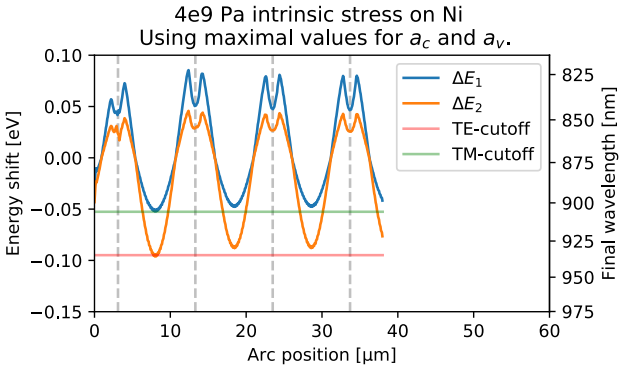

Figure 6.6: The split.

$S_{11} = 12.64 \cdot 10^{-12}\ \frac{\mathrm{m}^2}{\mathrm{N}}$, $S_{12} = -4.23 \cdot 10^{-12}\ \frac{\mathrm{m}^2}{\mathrm{N}}$, $S_{44} = -18.6 \cdot 10^{-12}\ \frac{\mathrm{m}^2}{\mathrm{N}}$, there can be solved for T using

$$E_{split,293K} = 0.02035\,\mathrm{eV} = \sqrt{\left(-2\,\mathrm{eV}(\frac{S_{11}+S_{12}}{2}T - S_{12}T)\right)^2 + (-4.8\,\mathrm{eV}d\frac{S_{44}}{4}T)^2} \tag{6.27}$$

$$\rightarrow T_{split,293K} = \pm 7.27 \cdot 10^8\ \frac{\mathrm{N}}{\mathrm{m}^2} \tag{6.28}$$

$$E_{shift,293K} = -0.0827\,\mathrm{eV} = -8.33\,\mathrm{eV}\left(2\frac{S_{11}+S_{12}}{2}T + S_{12}T\right)(\epsilon) \tag{6.29}$$

$$\rightarrow T_{shift,293K} = \pm 2.34 \cdot 10^9\ \frac{\mathrm{N}}{\mathrm{m}^2} \tag{6.30}$$

The fact that $T_{split,293\,\mathrm{K}} \neq T_{shift,293\,\mathrm{K}}$ means that the induced strain is not purely caused by an uniaxial shear stress. However, the split between the TE and TM modes is the same magnitude as the split found in the simulation. This can be seen on figure 6.6. As an interesting aside, this was reached by using the largest values for the deformation potentials found in literature, $a_c = -18.3\,\mathrm{eV}$, $a_v = -2.1\,\mathrm{eV}$. This means that the strain found in the simulations containing the intrinsic stress on Nickel was large enough to cause the splitting of the energy.

If it is assumed that the generally accepted values for the deformation potential are correct, $a_c = -7.17\,\mathrm{eV}$, $a_v = -1.16\,\mathrm{eV}$, a possible way of uniting the measured bandgap shift with the simulation would be to use strain induced by hydrostatic stress. This will not split the energy levels further, but will instead exclusively change the bandgap shift.

The uniaxial shear stress needed to induce the split is, as found in equation 6.28, $T_{split,293K} = 7.27 \cdot 10^8\ \frac{\mathrm{N}}{\mathrm{m}^2}$. This will give the energy shift

$$E_{shift,T} = (a_c + a_v)(2\frac{S_{11}+S_{12}}{2}T) = -8.33\,\mathrm{eV} \cdot 8.41 S_{11}\frac{\mathrm{m}^2}{\mathrm{N}} \cdot 7.27 \cdot 10^8\ \frac{\mathrm{N}}{\mathrm{m}^2} = -0.0509\,\mathrm{eV} \tag{6.31}$$

The hydrostatic stress must thus induce an energy shift of $-0.0827\,\mathrm{eV} - (-0.0509\,\mathrm{eV}) = -0.0317\,\mathrm{eV}$. For strain induced by hydrostatic stress, $\epsilon_{xx} = \epsilon_{yy} = \epsilon_{zz} = (S_{11} + 2S_{12})F$

$$-0.0317\,\mathrm{eV} = -8.33\,\mathrm{eV} \cdot 3\epsilon_{xx} \rightarrow \epsilon_{xx} = 1.27 \cdot 10^{(}-3) \rightarrow F = 3.401 \cdot 10^8\ \frac{\mathrm{N}}{\mathrm{m}^2} \tag{6.32}$$

Assuming that the strain leading to both the TE and TM cutoff are located at the same position in the cantilever waveguide, this gives a possible model for the strain and the forces causing it. As mentioned before, this thesis assumes that all of the intrinsic stress is placed on the Nickel layer. In this case, the shear stress term T would come from the Nickel layer seeking to contract, which transfers strain through the middle cantilever waveguide through the tether bridges.

With the TE and TM modes having the electric field along different directions, it is necessary to analyse how respectively the light and heavy holes interacts with the with the TE and TM waveguide modes. While it is obvious that there is a large band gap change, and that there is some kind of splitting in the electronic states making the band gap different for TE and TM modes, analyzing the electronic states of the GaAs cantilever waveguides using the measurements of respectively the TE and TM modes behavior in the waveguide is far from trivial for many reasons. First of all, the strain is not perfectly known, and, as can be seen in the simulation chapter, changes over the course of one waveguide. The absorption of light with and energies above the bandgap is extremely high, and thus having allowed absorption for even a small fraction of the waveguide length would be enough to completely extinguish the signal. Furthermore, if the strain is different thorough the cantilever, it is possible that there is one area where the strain is in such a way that the TE mode is cut off at $\lambda_{TE,1}$, while the TM mode is cutoff at $\lambda_{TM,1}$. At another place, the cutoffs might be $\lambda_{TE,2} > \lambda_{TE,1}$ and $\lambda_{TM,2} < \lambda_{TM,1}$. When measuring the spectrum this will show the TE cutoff wavelength as $\lambda_{TE,1}$ and the TM cutoff as $\lambda_{TM,2}$. Attempting to model the strain leading to this result would produce incorrect results. At best, the correct type of stress (biaxial, uniaxial shear etc) would be identified, while the wrong strain values would be found, while in the worst case scenario, the actual type of stress in the waveguide would not have any real solutions for the TE and TM cutoffs, and a wrong model would be identified.

It is reasonable to assume that any intrinsic stress lies on the Nickel layer, because otherwise ordinary suspended waveguides with grating couplers would also have a band gap change. Thus the strain in the simulation with the stress lying on Nickel can be used to gain insight into the mechanisms of the band gap shift. The simulation shows that the GaAs cantilever will, beside a shear strain term ϵ_{xy}, have strain seemingly induced by biaxial stress $\epsilon_{xx} = \epsilon_{yy} \approx -\epsilon_{zz}$, which is compressive in the xy-plane for the top of the waveguide, and tensile in the xy-plane at the bottom of the cantilever. The compressive strain at the top leads to a larger band gap and will not be treated here. Meanwhile, the small bandgap change at the middle is also not of interest. The large tensile strain at the bottom, however, is of interest, since that will result in a strong shift making the band-gap smaller.

Another complicating factor is that the strain can cause the HH states and LH states to hybridize or flip axes, which changes their selection rules for coupling between the holes and the TE and TM guided modes.[36]. The exact effect on shear strain on the hybridization and axis change of the bulk HH and LH states, and the following influence of the light-matter interaction for respectively the TE and TM guided modes is not well described in literature. A full understanding of the behavior of the light in the waveguide requires a deep insight into theory that, while fascinating, is beyond the scope of this thesis.

6.8 Summary

The waveguides were characterized for both the TE and TM modes at room and cryogenic temperatures. The bent cantilever couplers turned out to be extremely broadband, if low efficiency. A very unexpected find was the abrupt cutoff, which was shown to originate in a large bandgap change caused by the very high intrinsic strains in the GaAs cantilever waveguide.

Chapter 7

Conclusion and outlook

The aim of this thesis was to investigate a novel type of cantilever waveguide. The scope of this thesis was fluid, and changed continously as the thesis work progressed, and new discoveries were made. With the initial focus being piezo-electrical tuning of quantum dots embedded in the cantilever, later thesis work was focused on investigating the source of the transmission cutoff.

Upon investigation, the tips of the curved cantilever waveguides proved themselves to be extremely broadband, if inefficient, couplers, which were mechanically stable under drastic temperature changes.

It can be seen on figures 6.2 be seen how for wavelengths above the strained bandgap, the absorption efficiency doesn't immediately go to the maximum possible, but instead slowly slopes. It is possible that this is due to the Franz-Keldysh effect caused either by the Piezoelectric or the flexoelectric effect. Investigating whether this sloping effect was caused by Franz-Keldysh electroabsorption is an interesting possibility which could possibly shed further light on the size and nature of the intrinsic stress in the device, time constraints prevented an analysis of this topic.

Further possibilities involve the realization of a device capable of carrying out the piezoelectrical tuning of the quantum dots. While this was investigated using FEM models, the construction of such a device would be far from trivial, and was out of scope for this thesis. Other possibilities involve improving the efficiency of the coupler, for which a likely method would be to ensure that the orientation of the spot-size converter was completely vertical rather than slightly curved. Another possibility would be to optimize the fabrication routine, ensuring a higher yield of functioning devices.

Furthermore, additional insight into the nature of the strain-induced bandgap change could be obtained by fabricating and characterizing the circular cantilever waveguides with different radiuses of curvature. This would involve either adjusting the intrinsic stress on the Nickel layer, which changes with the deposition rate, or the thickness of said metal layer. Observing this bandgap change and comparing it with theoretical models would give a deeper understanding of the device.

Chapter 8

Bibliography

Bibliography

[1] J. O. Akinlami and A. O. Ashamu. "Optical properties of GaAs". In: *Journal of Semiconductors* 34.3 (Mar. 2013), p. 032002. ISSN: 1674-4926. DOI: 10.1088/1674-4926/34/3/032002. URL: https://iopscience.iop.org/article/10.1088/1674-4926/34/3/032002 (visited on 06/16/2021).

[2] *Analysis of Deformation in Solid Mechanics*. URL: https://www.comsol.com/multiphysics/analysis-of-deformation?parent=structural-mechanics-0182-192 (visited on 05/04/2021).

[3] A. Baca and C. Ashby. *Fabrication of GaAs Devices*. en. The Institution of Engineering and Technology, Michael Faraday House, Six Hills Way, Stevenage SG1 2AY, UK: IET, Jan. 2005. ISBN: 978-0-86341-353-7. DOI: 10.1049/PBEP006E. URL: https://digital-library.theiet.org/content/books/cs/pbep006e (visited on 05/05/2021).

[4] *Band structure and carrier concentration of Gallium Arsenide (GaAs)*. URL: http://www.ioffe.ru/SVA/NSM/Semicond/GaAs/bandstr.html#Temperature (visited on 06/16/2021).

[5] Benjah-bmm27. *English: Yellow balls are zinc and violet balls are sulphur in pure sphlareite crystal lattice unit cells*. URL: https://commons.wikimedia.org/wiki/File:Sphalerite-unit-cell-depth-fade-3D-balls.png (visited on 06/18/2021).

[6] J. Chovan and F. Uherek. "Photonic Integrated Circuits for Communication Systems". en. In: *Radioengineering* 27.2 (June 2018), pp. 357–363. ISSN: 1210-2512. DOI: 10.13164/re.2018.0357. URL: https://www.radioeng.cz/fulltexts/2018/18_02_0357_0363.pdf (visited on 06/19/2021).

[7] *Defining Curvilinear Coordinates for Anisotropic Materials — COMSOL Blog*. URL: https://www.comsol.com/blogs/defining-curvilinear-coordinates-anisotropic-materials/ (visited on 06/16/2021).

[8] Malin Edvardsson. *What is piezoelectricity?* en-us. URL: https://www.biolinscientific.com/blog/what-is-piezoelectricity (visited on 06/18/2021).

[9] *eFunda: Constitutive Transforms of Piezo Materials*. URL: https://www.efunda.com/materials/piezo/piezo_math/transforms.cfm (visited on 06/14/2021).

[10] Elsa Garmire and Alan Kost. *Semiconductors and Semimetals, 59: Nonlinear Optics In Semiconductors II*. English. OCLC: 437246307. Burlington: Elsevier, 1998. ISBN: 978-0-08-086457-0. URL: http://public.ebookcentral.proquest.com/choice/publicfullrecord.aspx?p=405280 (visited on 05/07/2021).

[11] David Guinovart-Sanjuán et al. "Simple closed-form expressions for the effective properties of multilaminated flexoelectric composites". en. In: *Journal of Engineering Mathematics* 127.1 (Apr. 2021), p. 4. ISSN: 0022-0833, 1573-2703. DOI: 10.1007/s10665-021-10096-5. URL: https://link.springer.com/10.1007/s10665-021-10096-5 (visited on 04/28/2021).

[12] D. R. Hartree. "THE ENIAC, AN ELECTRONIC CALCULATING MACHINE". en. In: *Nature* 157.3990 (Apr. 1946), pp. 527–527. ISSN: 0028-0836, 1476-4687. DOI: 10.1038/157527a0. URL: http://www.nature.com/articles/157527a0 (visited on 06/15/2021).

[13] Jiawang Hong and David Vanderbilt. "First-principles theory and calculation of flexoelectricity". en. In: *Physical Review B* 88.17 (Nov. 2013), p. 174107. ISSN: 1098-0121, 1550-235X. DOI: 10.1103/PhysRevB.88.174107. URL: https://link.aps.org/doi/10.1103/PhysRevB.88.174107 (visited on 05/04/2021).

[14] Chuanwei Huang and Lang Chen. "Negative Poisson's Ratio in Modern Functional Materials". en. In: *Advanced Materials* 28.37 (Oct. 2016), pp. 8079–8096. ISSN: 09359648. DOI: 10.1002/adma.201601363. URL: http://doi.wiley.com/10.1002/adma.201601363 (visited on 06/15/2021).

[15] Bruce A. Joyce and Dimitri D. Vvedensky. "Quantum Dots in the InAs/GaAs System". en. In: *Quantum Dots: Fundamentals, Applications, and Frontiers*. Ed. by Bruce A. Joyce et al. Vol. 190. Series Title: NATO Science Series. Berlin/Heidelberg: Springer-Verlag, 2005, pp. 1–26. ISBN: 978-1-4020-3313-1. DOI: 10.1007/1-4020-3315-X_1. URL: http://link.springer.com/10.1007/1-4020-3315-X_1 (visited on 06/19/2021).

[16] Charles Kittel. *Introduction to solid state physics*. 8th ed. Hoboken, NJ: Wiley, 2005. ISBN: 978-0-471-41526-8.

[17] Benny Lautrup. *Physics of continuous matter: exotic and everyday phenomena in the macroscopic world*. 2nd ed. Boca Raton: Taylor & Francis, 2011. ISBN: 978-1-4200-7700-1.

[18] Jia-ming Liu. *Photonic Devices*. 1st ed. Cambridge University Press, Apr. 2005. ISBN: 978-0-521-55195-3 978-0-521-55859-4 978-0-511-61425-5. DOI: 10.1017/CBO9780511614255. URL: https://www.cambridge.org/core/product/identifier/9780511614255/type/book (visited on 06/15/2021).

[19] Peter Lodahl. "Quantum-dot based photonic quantum networks". In: *Quantum Science and Technology* 3.1 (Jan. 2018), p. 013001. ISSN: 2058-9565. DOI: 10.1088/2058-9565/aa91bb. URL: https://iopscience.iop.org/article/10.1088/2058-9565/aa91bb (visited on 06/19/2021).

[20] Riccardo Marchetti et al. "Coupling strategies for silicon photonics integrated chips [Invited]". en. In: *Photonics Research* 7.2 (Feb. 2019), p. 201. ISSN: 2327-9125. DOI: 10.1364/PRJ.7.000201. URL: https://www.osapublishing.org/abstract.cfm?URI=prj-7-2-201 (visited on 05/06/2021).

[21] Paolo Minzioni et al. "Roadmap on all-optical processing". In: *Journal of Optics* 21.6 (June 2019), p. 063001. ISSN: 2040-8978, 2040-8986. DOI: 10.1088/2040-8986/ab0e66. URL: https://iopscience.iop.org/article/10.1088/2040-8986/ab0e66 (visited on 06/19/2021).

[22] Mohammad Ali Mohammad et al. "Fundamentals of Electron Beam Exposure and Development". en. In: *Nanofabrication*. Ed. by Maria Stepanova and Steven Dew. Vienna: Springer Vienna, 2012, pp. 11–41. ISBN: 978-3-7091-0423-1 978-3-7091-0424-8. DOI: 10.1007/978-3-7091-0424-8_2. URL: http://link.springer.com/10.1007/978-3-7091-0424-8_2 (visited on 05/26/2021).

[23] E Moiseeva et al. "Single-mask microfabrication of three-dimensional objects from strained bimorphs". In: *Journal of Micromechanics and Microengineering* 17.9 (Sept. 2007), N63–N68. ISSN: 0960-1317, 1361-6439. DOI: 10.1088/0960-1317/17/9/N01. URL: https://iopscience.iop.org/article/10.1088/0960-1317/17/9/N01 (visited on 04/19/2021).

[24] E. Moiseeva et al. "Single-mask microfabrication of three-dimensional objects from strained bimorphs". en. In: *Journal of Micromechanics and Microengineering* 17.9 (Aug. 2007). Publisher: IOP Publishing, N63. ISSN: 0960-1317. DOI: 10.1088/0960-1317/17/9/N01. URL: https://iopscience.iop.org/article/10.1088/0960-1317/17/9/N01/meta (visited on 04/19/2021).

[25] *Optical properties of Gallium Arsenide (GaAs)*. URL: http://www.ioffe.ru/SVA/NSM/Semicond/GaAs/optic.html (visited on 06/18/2021).

[26] Sangyoon Paik et al. "Near-field sub-diffraction photolithography with an elastomeric photomask". en. In: *Nature Communications* 11.1 (Dec. 2020), p. 805. ISSN: 2041-1723. DOI: 10.1038/s41467-020-14439-1. URL: http://www.nature.com/articles/s41467-020-14439-1 (visited on 06/17/2021).

[27] Emmanuel Rosencher and Borge Vinter. *Optoelectronics*. Trans. by P. G. Piva. 1st ed. Cambridge University Press, May 2002. ISBN: 978-0-521-77129-0 978-0-521-77813-8 978-0-511-75464-7. DOI: 10.1017/CBO9780511754647. URL: https://www.cambridge.org/core/product/identifier/9780511754647/type/book (visited on 05/03/2021).

[28] Rumble Jr et al. *CRC handbook of chemistry and physics: a ready-reference book of chemical and physical data*. English. OCLC: 1126006278. 2019. ISBN: 978-1-138-36729-6.

[29] T. E. Schlesinger. "Gallium Arsenide". en. In: *Encyclopedia of Materials: Science and Technology*. Ed. by K. H. Jürgen Buschow et al. Oxford: Elsevier, Jan. 2001, pp. 3431–3435. ISBN: 978-0-08-043152-9. DOI: 10.1016/B0-08-043152-6/00612-4. URL: https://www.sciencedirect.com/science/article/pii/B0080431526006124 (visited on 06/18/2021).

[30] Steven H. Simon. *The Oxford solid state basics*. 1st ed. OCLC: ocn853504907. Oxford: Oxford University Press, 2013. ISBN: 978-0-19-968077-1 978-0-19-968076-4.

[31] *Stress Transformations*. URL: https://www.continuummechanics.org/stressxforms.html (visited on 06/15/2021).

[32] Yongke Sun, Scott E. Thompson, and Toshikazu Nishida. *Strain Effect in Semiconductors: Theory and Device Applications*. en. Springer US, 2010. ISBN: 978-1-4419-0551-2. DOI: 10.1007/978-1-4419-0552-9. URL: https://www.springer.com/gp/book/9781441905512 (visited on 11/17/2020).

[33] Aslı D. Uğurlu et al. "Suspended Spot-Size Converters for Scalable Single-Photon Devices". en. In: *Advanced Quantum Technologies* 3.2 (Feb. 2020), p. 1900076. ISSN: 2511-9044, 2511-9044. DOI: 10.1002/qute.201900076. URL: https://onlinelibrary.wiley.com/doi/abs/10.1002/qute.201900076 (visited on 06/16/2021).

[34] Ravitej Uppu et al. "Scalable integrated single-photon source". en. In: *Science Advances* 6.50 (Dec. 2020), eabc8268. ISSN: 2375-2548. DOI: 10.1126/sciadv.abc8268. URL: https://advances.sciencemag.org/lookup/doi/10.1126/sciadv.abc8268 (visited on 06/19/2021).

[35] Ying Wang et al. "Electroabsorption in gated GaAs nanophotonic waveguides". en. In: *Applied Physics Letters* 118.13 (Mar. 2021), p. 131106. ISSN: 0003-6951, 1077-3118. DOI: 10.1063/5.0039373. URL: https://aip.scitation.org/doi/10.1063/5.0039373 (visited on 06/07/2021).

[36] Xueyong Yuan et al. "Uniaxial stress flips the natural quantization axis of a quantum dot for integrated quantum photonics". In: *Nature Communications* 9.1 (Dec. 2018). arXiv: 1710.03962, p. 3058. ISSN: 2041-1723. DOI: 10.1038/s41467-018-05499-5. URL: http://arxiv.org/abs/1710.03962 (visited on 06/09/2021).

[37] P V Yudin and A K Tagantsev. "Fundamentals of flexoelectricity in solids". In: *Nanotechnology* 24.43 (Nov. 2013), p. 432001. ISSN: 0957-4484, 1361-6528. DOI: 10.1088/0957-4484/24/43/432001. URL: https://iopscience.iop.org/article/10.1088/0957-4484/24/43/432001 (visited on 04/29/2021).

[38] Xiaoyan Zhou et al. "High-efficiency shallow-etched grating on GaAs membranes for quantum photonic applications". In: *Applied Physics Letters* 113.25 (Dec. 2018). Publisher: American Institute of Physics, p. 251103. ISSN: 0003-6951. DOI: 10.1063/1.5055622. URL: https://aip.scitation.org/doi/10.1063/1.5055622 (visited on 11/17/2020).